# Paleoceanography and Paleoclimatology®

**Correspondence to:**

R. P. Acosta,
racosta6@gmu.edu

# A Model-Data Comparison of the Hydrological Response to Miocene Warmth: Leveraging the MioMIP1 Opportunistic Multi-Model Ensemble

R. P. Acosta[1], N. J. Burls[1], M. J. Pound[2], C. D. Bradshaw[3,4], A. M. De Boer[5], N. Herold[6], M. Huber[7], X. Liu[7], Y. Donnadieu[8], A. Farnsworth[9], A. Frigola[10,11], D. J. Lunt[9], A. S. von der Heydt[12], D. K. Hutchinson[13], G. Knorr[14], G. Lohmann[14], A. Marzocchi[15], M. Prange[10], A. C. Sarr[8,16], X. Li[17], and Z. Zhang[17,18]

[1]Department of Atmospheric, Ocean and Earth Sciences, Center for Ocean-Land Atmosphere Studies, George Mason University, Fairfax, VA, USA, [2]Department of Geography and Environmental Sciences, Northumbria University, Newcastle, UK, [3]Met Office Hadley Centre, Exeter, UK, [4]The Global Systems Institute, University of Exeter, Exeter, UK, [5]Department of Geological Sciences, Bolin Center for Climate Research, Stockholm University, Stockholm, Sweden, [6]Applied Climate Science Pty Ltd., Adelaide, SA, Australia, [7]Department of Earth, Atmospheric, and Planetary Sciences, Purdue University, West Lafayette, IN, USA, [8]Aix Marseille University, CNRS, IRD, Coll France, INRA, CEREGE, Aix en Provence, France, [9]School of Geographical Sciences, University of Bristol, Bristol, UK, [10]MARUM—Center for Marine Environmental Sciences, University of Bremen, Bremen, Germany, [11]Barcelona Supercomputing Center, Barcelona, Spain, [12]Department of Physics, Faculty of Science, Institute for Marine and Atmospheric Research, Utrecht University, Utrecht, The Netherlands, [13]Climate Change Research Centre, University of New South Wales, Sydney, Australia, [14]Alfred Wegener Institute Helmholtz Centre for Polar and Marine Research, Bremerhaven, Germany, [15]National Oceanography Centre, Southampton, UK, [16]Université Grenoble Alpes, Université Savoie Mont Blanc, CNRS, IRD, Université Gustave Eiffel, ISTerre, Grenoble, France, [17]Department of Atmospheric Science, School of Environmental Studies, China University of Geoscience, Wuhan, China, [18]NORCE Norwegian Research Centre, Bjerknes Centre for Climate Research, Bergen, Norway

**Abstract** The Miocene (23.03–5.33 Ma) is recognized as a period with close to modern-day paleogeography, yet a much warmer climate. With large uncertainties in future hydroclimate projections, Miocene conditions illustrate a potential future analog for the Earth system. A recent opportunistic Miocene Model Intercomparison Project 1 (MioMIP1) focused on synthesizing published Miocene climate simulations and comparing them with available temperature reconstructions. Here, we build on this effort by analyzing the hydrological cycle response to Miocene forcings across early-to-middle (E2MMIO; 20.03–11.6 Ma) and middle-to-late Miocene (M2LMIO; 11.5–5.33 Ma) simulations with $CO_2$ concentrations ranging from 200 to 850 ppm and providing a model-data comparison against available precipitation reconstructions. We find global precipitation increases by ~2.1 and 2.3% per degree of warming for E2MMIO and M2LMIO simulations, respectively. Models generally agree on a wetter than modern-day tropics; mid and high-latitude, however, do not agree on the sign of subtropical precipitation changes with warming. Global monsoon analysis suggests most monsoon regions, except the North American Monsoon, experience higher precipitation rates under warmer conditions. Model-data comparison shows that mean annual precipitation is underestimated by the models regardless of $CO_2$ concentration, particularly in the mid- to high-latitudes. This suggests that the models may not be (a) resolving key processes driving the hydrological cycle response to Miocene boundary conditions and/or (b) other boundary conditions or processes not considered here are critical to reproducing Miocene hydroclimate. This study highlights the challenges in modeling and reconstructing the Miocene hydrological cycle and serves as a baseline for future coordinated MioMIP efforts.

**Plain Language Summary** This study looks at Earth's hydrological cycle during the Miocene (23–5 million years ago). During this period, the Earth's climate was 3–7°C warmer than today, with carbon dioxide ($CO_2$) estimates ranging between 400 and 850 ppm. Understanding how the hydrological cycle responded during warmer climate conditions can give us insight into what might happen as the Earth gets warmer. We analyzed a suite of Miocene paleoclimate simulations with different $CO_2$ concentrations in the atmosphere and compared them against fossil plant data, which gives an estimate of the average annual rainfall during the period. We found that during the Miocene global rainfall increased by about 2.1%–2.3% for each degree of warming. The models agree that the tropics, mid- and high-latitude, became wetter than they are today but have lower agreement on whether subtropical areas got wetter or drier as they warmed. Compared to proxies, models

consistently underestimated how much rain fell in a year, especially in the mid- to high-latitude. This illustrates the challenges in reconstructing the Miocene's hydrological cycle and suggests that the models might not fully capture the range of uncertainties associated with changes in the hydrological cycle due to warming or other factors that differentiated the Miocene.

## 1. Introduction

The availability of multi-model ensemble-derived projections, such as those found in the Coupled Model Intercomparison Project (CMIP) has increased our understanding of possible future global and regional precipitation and drought patterns (Douville et al., 2021; Ukkola et al., 2020). However, considerable uncertainty still exists in end-of-the-century climate model projections and, therefore, how the hydrological cycle will change under warmer conditions (Mann, 2021). Even as CMIP models become more sophisticated, model agreement over hydrological patterns of change over many parts of the world still remains low (Douville et al., 2021; Solomon et al., 2009). Studying past warm greenhouse climates like the Miocene provides insight into how the hydrological cycle responds to changes in multiple boundary conditions such as greenhouse gases and paleogeography and offers independent means to evaluate model skill (Mann, 2021; Tierney et al., 2020; Zhu et al., 2021). If differences in boundary conditions such as continental configuration, topography, and vegetation are considered, the Miocene can be a powerful analog for future climate change.

The Miocene (23.03–5.33 Ma) is recognized as a period much warmer than modern-day. Early-to-middle Miocene paleobotanical records illustrated a much wetter climate than the modern-day with megathermal tropical forests (Acosta et al., 2022; Jaramillo et al., 2010; Morley, 2011; Pound et al., 2012), and expanded habitable zones for large leaf-eating mammalians (Steinthorsdottir et al., 2021; Yu et al., 2014). Within the Miocene is the Miocene Climatic Optimum (MCO; 16.75–14.5 million years ago), which represents the peak of Miocene global warmth with estimated global mean surface temperature (GMST) from both aquatic and terrestrial proxies at ∼23°C, and as high as ∼25°C when based only on sea surface temperature (SST) proxies (Burls et al., 2021). Reconstructions for atmospheric $CO_2$ during the MCO range from 400 to 1,500 ppm (Rae et al., 2021; Steinthorsdottir et al., 2021), and hence, the MCO is viewed as a potential analog for the end of the 23rd-century projection under Shared Socioeconomic Pathways 3 and 4. Climate reconstruction of the MCO reveals warmer conditions than the Pliocene (∼3 Ma) but not as extreme as the Eocene (∼50 Ma) (Rae et al., 2021; Westerhold et al., 2020). However, for such a crucial period, a proper analysis of the Miocene hydroclimate through data-model and inter-model comparison has yet to be presented, leading to gaps in our understanding.

Changes in GMST, polar amplified warming, and the equator-to-pole temperature gradient are critical in governing the global hydrological cycle (e.g., Allan et al., 2020; Burls & Fedorov, 2017; Frieling et al., 2017; Held & Soden, 2006; Pierrehumbert, 2002). Under warm climate conditions, the equator-to-pole temperature gradient is expected to be lower (Gaskell et al., 2022; Huber & Caballero, 2011; Liu et al., 2022; Lunt et al., 2012; Pierrehumbert, 2002), which has been demonstrated by syntheses of Miocene ocean and terrestrial surface temperature proxies (Burls et al., 2021; Goldner et al., 2014). Initially recognized in Goldner et al. (2014) and reiterated by the Miocene Model Intercomparison Project 1 "MIP of opportunity" (MioMIP1) (Burls et al., 2021), the simulations with moderately high $CO_2$ concentrations (<560 ppm) simulated SST based GMSTs that are too cold compared to Miocene proxy reconstructions of 25°C (Burls et al., 2021; Herbert et al., 2022). Furthermore, warming in the extra-tropics, specifically in the North Atlantic, is still underestimated by the models that maintain a meridional temperature gradient higher than proxy estimates (Burls et al., 2021; Super et al., 2020). Only when $CO_2$ concentrations are set to 560 or 850 ppm do the MioMIP1 models begin to reproduce the reconstructed GMST estimates and partially capture polar amplified warming. Conversely, however, at above 560 ppm, most modeled tropical SSTs become too warm relative to proxy estimated SSTs (Burls et al., 2021), although some models, especially latter versions of NCAR Community Earth System Model (CESM), can simultaneously match most tropical and high latitude SSTs with sufficient greenhouse gas forcing (Gaskell et al., 2022; Liu et al., 2022). Nonetheless, the MioMIP models predominantly simulate strong equator-to-pole temperature gradients and still underestimate the warming across the North Atlantic (Burls et al., 2021). The strong simulated equator-to-pole temperature gradient is thought to be linked to land cover types such as vegetation (Bradshaw et al., 2015; Pound et al., 2012), land-ice distribution (Goldner et al., 2014; Singh et al., 2016), orbital forcing (Goldner et al., 2014; Ladant et al., 2014), cloud-aerosol interaction (Erfani & Burls, 2019; Heavens et al., 2012), and ocean circulation (Fedorov et al., 2015). Nevertheless, the difficulty of the MioMIP1 models to reconcile

such weak equator to pole temperature gradients will ultimately influence the meridional moisture transport and precipitation distribution.

While many studies focus on Miocene warming, its hydroclimate remains poorly characterized. We first look at the sensitivity of the Miocene hydroclimate to non-$CO_2$-related boundary conditions. Second, similar to the Eocene DeepMIP (EoMIP) hydrological cycle analysis (Carmichael et al., 2016; Cramwinckel et al., 2023), we explore the hydroclimate response of the Miocene under a wide range of plausible $CO_2$ scenarios, by analyzing the strength of the global, tropical, subtropical, mid-latitude, and high-latitude hydrological cycle (Held & Soden, 2006; Pendergrass, 2020). We perform a moisture transport analysis on multi-model means and individual models. We also provide a brief analysis on the Intertropical Convergence Zone (ITCZ), and global monsoon changes during the Miocene. A decade earlier, seminal middle Miocene modeling work (Herold et al., 2011, 2010) identified mean annual precipitation (MAP) model-data discrepancy using the NCAR CCSM3 model and demonstrated how CCSM3 underestimated proxy-derived precipitation signals. As an update to Herold et al. (2011, 2010) our study increases the number of precipitation records using previously published and updated Miocene paleobotanical datasets (Burls et al., 2021; Pound et al., 2012, 2011) and compares them to the MioMIP1 models, which includes the simulations used in Herold et al. (2011, 2010). In-depth pointwise model-data analysis of MAP using plant-fossil records and paleoclimate simulations from the MioMIP1 is conducted.

## 2. Methods

### 2.1. Miocene Climate Simulations

MioMIP1 is an opportunistic intercomparison project that makes use of preexisting Miocene simulations performed by individual climate modeling groups to tackle specific scientific problems such as the impact of paleo-$CO_2$, changes in paleogeography like the opening and closing of gateways, Antarctic ice-sheet extent and height, changes in regional topography, and land-surface changes such as vegetation and soil distribution. Burls et al. (2021) present initial synthesis results that focus on surface temperature and energy budget and assess the degree of model agreement and differences across a large spread of $CO_2$ configurations. Unlike coordinated MIPs, the Miocene boundary conditions in this opportunistic MIP are not standardized and differ across modeling efforts. Differences in Miocene surface warming across the model ensemble are due to not only model differences in climate feedback strengths but also the spread in imposed boundary conditions. In the global mean, Burls et al. (2021) found that prescribed $CO_2$ is the dominant factor controlling global warming across the MioMIP1 ensemble, while Miocene paleogeography and ice sheets raise the GMST by ∼2°C compared to the PI on average across the multi-model mean.

Leveraging the MioMIP1 ensemble compiled by Burls et al. (2021), here we investigate the Miocene hydroclimate. The simulations used in this study include the original MioMIP ensemble of Burls et al. (2021), with the addition of three new CESM1-CAM5 early-to-middle Miocene simulations (Acosta et al., 2022; Gaskell et al., 2022) and three new IPSL-CM5A2 middle-to-late Miocene simulations (Sarr et al., 2022; Sepulchre et al., 2020). In total, there are 47 model runs with 34 early-to-middle Miocene (referred to as E2MMIO) and 13 middle-to-late Miocene (referred to as M2LMIO) simulations (Table 1). Each paleoclimate simulation is accompanied by a complementary Preindustrial simulation (referred to as PI). Ensemble means are calculated for different $CO_2$ ranges, with each range denoted by a single $CO_2$ value: 200–300 ppm as 280, 350–450 ppm as 400, 500–600 ppm as 560, and 800–850 ppm as 850. We refer the reader to Table 1 for a brief description of each simulation and to Burls et al. (2021) for a more detailed description.

### 2.2. Paleobotanical Data

Proxy estimates of MAP were derived from previously published paleobotanical records (Bradshaw et al., 2012; Pound et al., 2012) and incorporated additional new datasets recently updated in Burls et al. (2021). Here, we have also divided the data into the same early-to-middle and middle-to-late Miocene periods that are assumed for the model simulations (Figure 1 and Supporting Information S1). Plant fossils are widely preserved in the geological records and are primarily governed by the regional climate (temperature and precipitation) and past geography (soil type, topographic history), which is ideal for reconstructing past hydroclimate systems. A wide variety of fossil records were used to compile MAP, which includes seeds, pollen, spores, leaves, woods, and paleosols. Extraction of climate signals was estimated by using the coexistence approach (Utescher et al., 2014) and Climate

**Table 1**
*MioMIP1 Model Description*

| | Target time period | ATM model resolution | $CO_2$ configurations | Original citation |
|---|---|---|---|---|
| *E2MMIO models* | | | | |
| CCSM3-NH3 | 20–14 Ma | T31–3.75° | 355, 560 | Herold et al. (2011) |
| CCSM3 MMCO | MMCO | T42–2.8° | 200, 400 | Frigola et al. (2018) |
| CCSM3 MMG | MMG | T42–2.8° | 200, 400 | Frigola et al. (2018) |
| CCSM4 (CAM4) | 20–14 Ma | 1.9° × 2.5° | 400 | Goldner et al. (2014) |
| CESM1 (CAM5) | 20–14 Ma | 1.9° × 2.5° | 400 | Dicks (2019) |
| CESM1 (CAM5) | 20–14 Ma | 1.9° × 2.5° | 280, 560, 840 | Acosta et al. (2022) |
| COSMOS | Middle Miocene | 3.75° × 3.75° | 278, 450 | |
| HadCM3L 90SLE | Middle Miocene | 3.75° × 2.5° | 280, 400, 560, 850 | Bradshaw et al. (2021) |
| HadCM3L 55SLE | Middle Miocene | 3.75° × 2.5° | 280, 400, 560, 850 | Bradshaw et al. (2021) |
| HadCM3L NoICE | Middle Miocene | 3.75° × 2.5° | 280, 400, 560, 850 | Bradshaw et al. (2021) |
| HadCM3L Langhian | Langhian | 3.75° × 2.5° | 280, 400, 560 | Farnsworth et al. (2019a, 2019b) |
| IPSLCM | 20 Ma | 3.75° × 1.875° | 420, 560, 840 | |
| IPSLCM NoGIS | 20 Ma | 3.75° × 1.875° | 560 | |
| NorESM | 20 Ma | T31–3.75° | 350, 560 | Zhang et al. (2014) |
| *M2LMIO models* | | | | |
| COSMOS | Tortonian | 3.75° × 3.75° | 278, 450 | Knorr et al. (2011), Stärz et al. (2017) |
| COSMOS ICEQ | Tortonian | 3.75° × 3.75° | 278, 450 | Knorr and Lohmann (2014) |
| HadCM3L | 11–5 Ma | 3.75° × 2.5° | 280, 400 | Bradshaw et al. (2015) |
| HadCM3L Tortonian | Tortonian | 3.75° × 2.5° | 400 | Farnsworth et al. (2019a, 2019b) |
| HadCM3L Messinian | Messinian | 3.75° × 2.5° | 400 | Farnsworth et al. (2019a, 2019b) |
| NorESM | 11–5 Ma | | 420, 560 | Zhang et al. (2014) |
| IPSLCM | 11–5 Ma | 3.75° × 1.9° | 280, 400, 560 | Sarr et al. (2022) |

Leaf Analysis Multivariate Program (Spicer et al., 2021) for plant records (Gibson et al., 2022). Error margins and uncertainty ranges were taken from previously published work (Bradshaw et al., 2012; Pound et al., 2012).

### 2.3. Analysis (Bias, Moisture Budget, Monsoon Criteria, and Model-Data Comparison)

Our analysis of Miocene hydroclimate, as simulated by the MioMIP1 ensemble, consists of four main parts: (1) Miocene hydroclimate compared to preindustrial focusing on precipitation change; (2) a zonal-mean moisture budget analysis; (3) evaluation of simulated monsoonal precipitation characteristics; and (4) a model-data comparison of Miocene precipitation patterns.

To understand changes in the hydrological cycle with respect to increasing $CO_2$, we investigate changes in precipitation ($P$) versus GMST. To identify robust emergent precipitation patterns, we calculate the mean percent change in precipitation relative to the PI, with positive change representing wetter than PI, and negative change representing drier than PI. For spatial features, we define robust wet and dry signals where 80% of the models agree on the sign of change. Additionally, we analyze precipitation minus evaporation ($E$). Since $P - E$ is balanced by the convergence of atmospheric moisture transport ($vq$) integrated from the surface to the top of the troposphere, we extract the implied moisture transport from P-E, as shown in Equation 1.

$$P - E = -\nabla \frac{1}{g} \int_0^{p_s} vq \cdot dp \tag{1}$$

where $\nabla$ is the "del" vector differential operator comprised of the zonal and meridional partial derivatives, $g$ is gravity, $v$ is the horizontal wind vector, $q$ is humidity, and $dp$ is the change in pressure with respect to height.
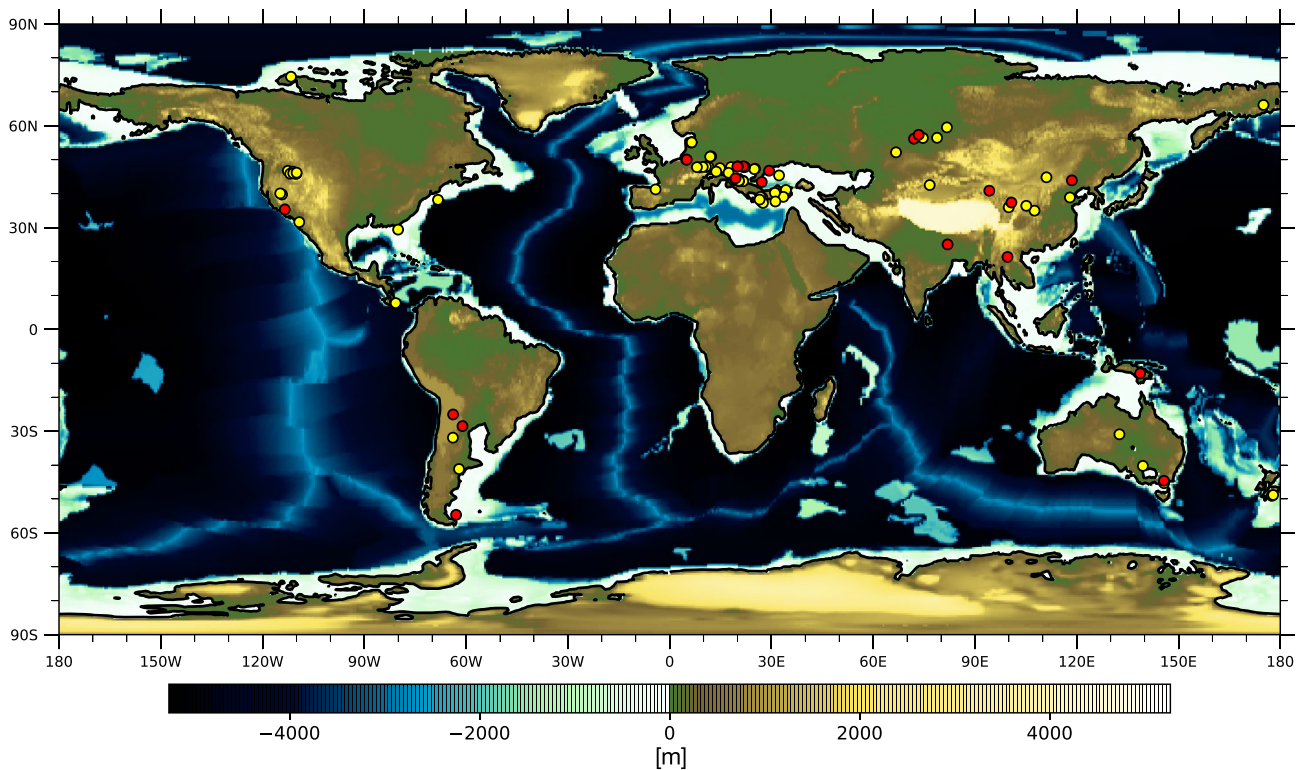
**Figure 1.** Middle Miocene paleogeography adapted from Herold et al. (2011). Circle symbols represent location of plant fossil assemblages recompiled in Burls et al. (2021) with early-to-middle (20–11.6 Ma) sites in yellow and middle-to-late (11.5–6 Ma) in red. Samples are adjusted according to their paleo latitude and longitude locations.

A modern-day precipitation seasonality index was used to identify the changes in regional monsoon systems (Wang & Ding, 2006). This method uses the percent of total precipitation occurring during extended Boreal summer months May, June, July, August, and September (MJJAS) and Austral summer months November, December, January, February, and March (NDJFM) as a measure of how much seasonal rainfall occurs in a region. For our analysis, we used the criteria of 55% of summer to annual precipitation to designate a monsoonal region. We then use the newly created monsoonal regions to analyze the monthly precipitation cycle.

To quantitatively determine the MAP model-data comparison, we used the same methodology as Bradshaw et al. (2012) and Burls et al. (2021). The method uses uncertainty overlap to define where model-data values match. The precipitation bias is defined as nonoverlapping values between the reconstructed and modeled uncertainty ranges, respectively.

$$\text{bias}_{\text{Model underestimate}} = -(\text{obs}_{\text{min}} - \text{Mod}_{\text{max}})$$

$$\text{or}$$

$$\text{bias}_{\text{Model overestimate}} = \text{Mod}_{\text{min}} - \text{Obs}_{\text{max}} \tag{2}$$

For the proxy data, the minimum-maximum MAP estimates for each site are used as the range of uncertainty. For the models, the MAP values across all neighboring grid points of the proxy site location are used as the range of uncertainty. We define positive values as models overestimating and negative values as underestimating observed values. For an overall metric for the level of model-data agreement, we calculate the global root-mean-squared error of the bias (RMSB).

$$\text{RMSB} = \sqrt{\overline{\text{bias}^2}} \tag{3}$$

In addition to a global RMSB, regional and seasonal RMSBs are separated into five regions: North America, South America, Europe, Eurasia, and Australia.

## 3. Results

### 3.1. Preindustrial Multi-Model Mean

We begin by comparing the MAP of the multi-model mean of all PI simulations (Table 1) against the modern-day (1979–2008) observations-based product, Global Precipitation Climatology Project (GPCP) (Adler et al., 2003). We note since GPCP represents a modern-day climate, simulated PI rainfall is likely to produce a lower precipitation rate than GPCP due to the reduced greenhouse gas concentrations implemented in the simulations. We primarily use this comparison to show the general global precipitation and aridity patterns are captured by the PI multi-model mean (Figures 2a and 2b). In general, the PI multi-model mean simulates modern MAP patterns, except for excess precipitation rates occurring over terrestrial regions such as Central Asia, Southern Africa, Central Australia, and western coastal regions of South America, and over ocean basins such as the south equatorial Atlantic Basin, cross-equatorial Arabian Sea, and maritime Southeast Asia Sea (Figure 2c). In contrast, the PI multi-model mean is drier than GPCP over the Amazon Basin, southern regions of South America, Central America, Western and Eastern coastal regions of North America, and Indo-Asia (Figure 2c). The PI multi-model mean reproduces the well-known double ITCZ precipitation band (Lin, 2007; Oueslati & Bellon, 2015) occurring over the Pacific Basin (Figure 2a vs. Figure 2b) and is pronounced in the zonal mean fields (see Section 3.2.2 for details).

### 3.2. Miocene Hydroclimate in MioMIP1 Models

#### 3.2.1. MioMIP1 Models Versus Preindustrial

To first evaluate the broad MAP patterns, we assess the multi-model mean of the simulated precipitation changes relative to the PI simulations for the E2MMIO and M2LMIO simulations, respectively (Figures 3 and 4). We also include a zonal mean analysis of MAP to understand the latitudinal structure of the precipitation changes. The individual model comparisons are in the Supplementary document (Figures S1 and S2 in Supporting Information S1).

The increase in global mean temperature in response to elevated atmospheric $CO_2$ concentrations typically enhances global and regional precipitation and evaporation rates, while the addition of non-modern boundary conditions, such as paleogeography and land surface properties, can lead to complex regional precipitation changes (Carmichael et al., 2016). By analyzing E2MMIO and M2LMIO 280 ppm simulations (Figures 3a and 4a), we can highlight the impact of non-$CO_2$ related boundary conditions on the hydroclimate. Terrestrial precipitation rates over western North America, Eastern Europe, Northern Africa, Indo-Asia, and Northeast Asia for the E2MMIO and M2LMIO 280 ppm simulations are higher than PI. While over the ocean subtropical Pacific Ocean, Southern Hemisphere subtropical Atlantic Ocean, and Indian Ocean are much wetter than PI. We can expect both the E2MMIO and M2LMIO 280 ppm multi-model means to be wetter than PI in most regions since differences in non-$CO_2$ boundary conditions alone warm the Miocene simulations by ∼2°C. The regions that are drier than PI simulations occur over Eastern North America, Central Asia, Southern Africa, Central America, and the majority of South America. Differences in the plate tectonic reconstructions (Lunt et al., 2016), such as the open Central American Seaway, could be contributing to the lowered precipitation rates found over Central America (Brierley & Fedorov, 2016). Lower elevations in the Miocene, such as those found in South America and Central Asia, could also lower precipitation over the region (Acosta et al., 2022; Farnsworth et al., 2019a, 2019b). In addition, the lack of wetlands in various simulations could also reduce regional moisture sources and lower regional precipitation rates (Fu et al., 2021; Jeffery et al., 2012).

In general, increasing $CO_2$ concentrations result in increased precipitation rates in regions where precipitation is already high under low $CO_2$ concentrations, that is, the deep tropics and mid- to high-latitudes, and leads to slightly reduced precipitation in the subtropics (Figures 3 and 5a). Enhanced E2MMIO precipitation patterns emerge under all $CO_2$ concentrations over western North America, Northern Africa, Northern Eurasia, Northern Australia, and Western Amazon Basin. Drier than PI patterns emerge under all $CO_2$ configurations in northern South America, the eastern Amazon Basin, Southern Africa, maritime Southeast Asia Sea, Arabian Sea, and Himalayan-Tibetan and Andean Mountains. At high $CO_2$ concentrations (560 and 850 ppm), high-latitude (60°–90°N and S) precipitation rates substantially increase (Figures 3c and 3d).

Analysis of high $CO_2$ (400 and 560 ppm) M2LMIO multi-model mean shows wetter than PI conditions over western North America, Northern and Eastern Africa, Greenland, northern Europe, and the Indian Ocean. Drier than PI conditions persist over Central America, the Tibetan region, and southern parts of South America (Figure 4). New precipitation patterns emerge under higher $CO_2$ concentrations, especially above 560 ppm. For example, northern parts of South America, Southern Africa, Indo-Asia, and Australia switch from drying to wetting
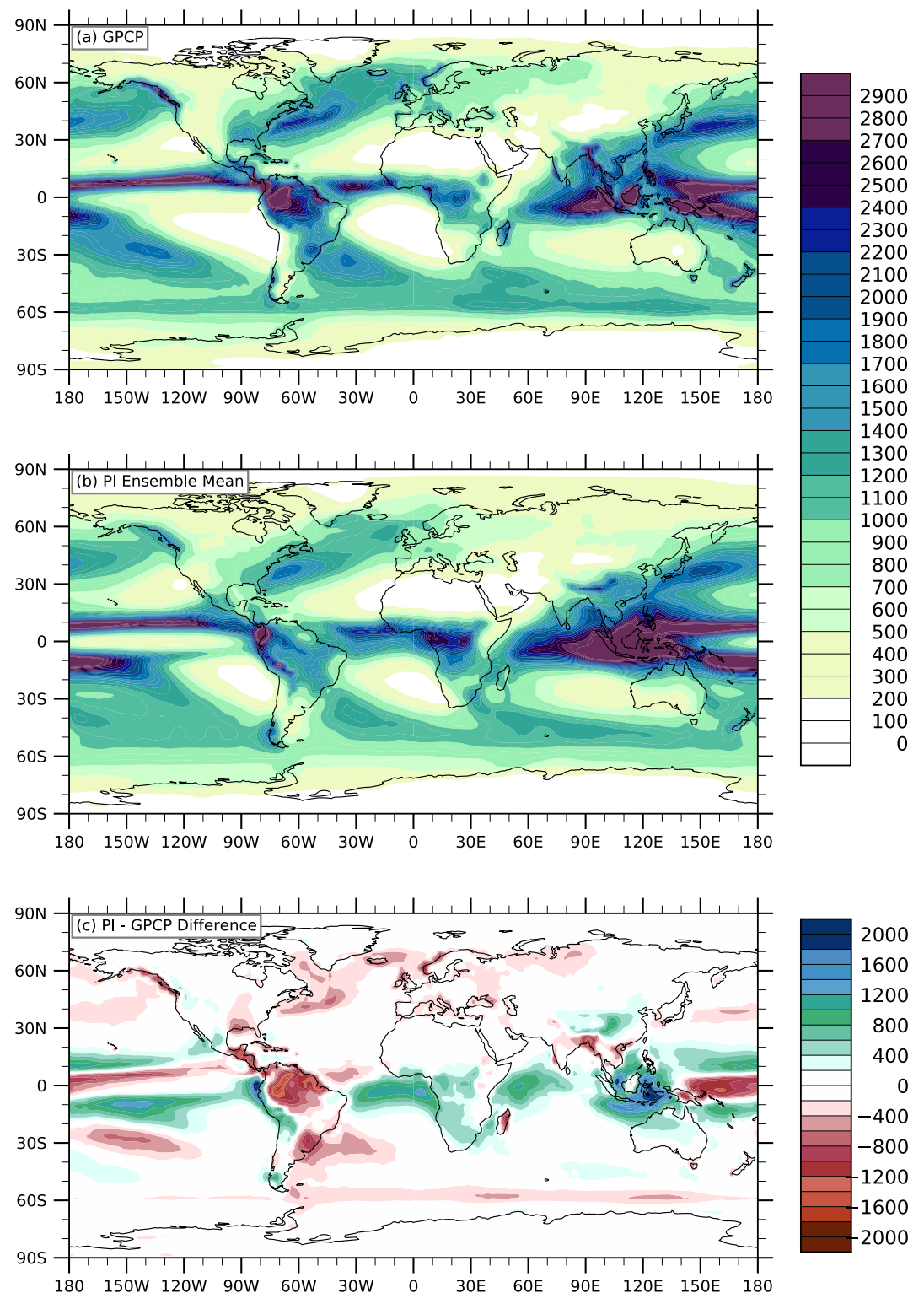
**Figure 2.** Annual mean precipitation (mm) comparison between observation Global Precipitation Climatology Project and Preindustrial multi-model mean.

conditions. We suspect that the low number of ensemble members in the M2LMIO 560 ppm multi-model mean could be strongly influencing the precipitation patterns between the low and high $CO_2$ ensemble mean (Figure S2 in Supporting Information S1). For example, Indo-Asia, Southern Africa, northern South America, and Australia
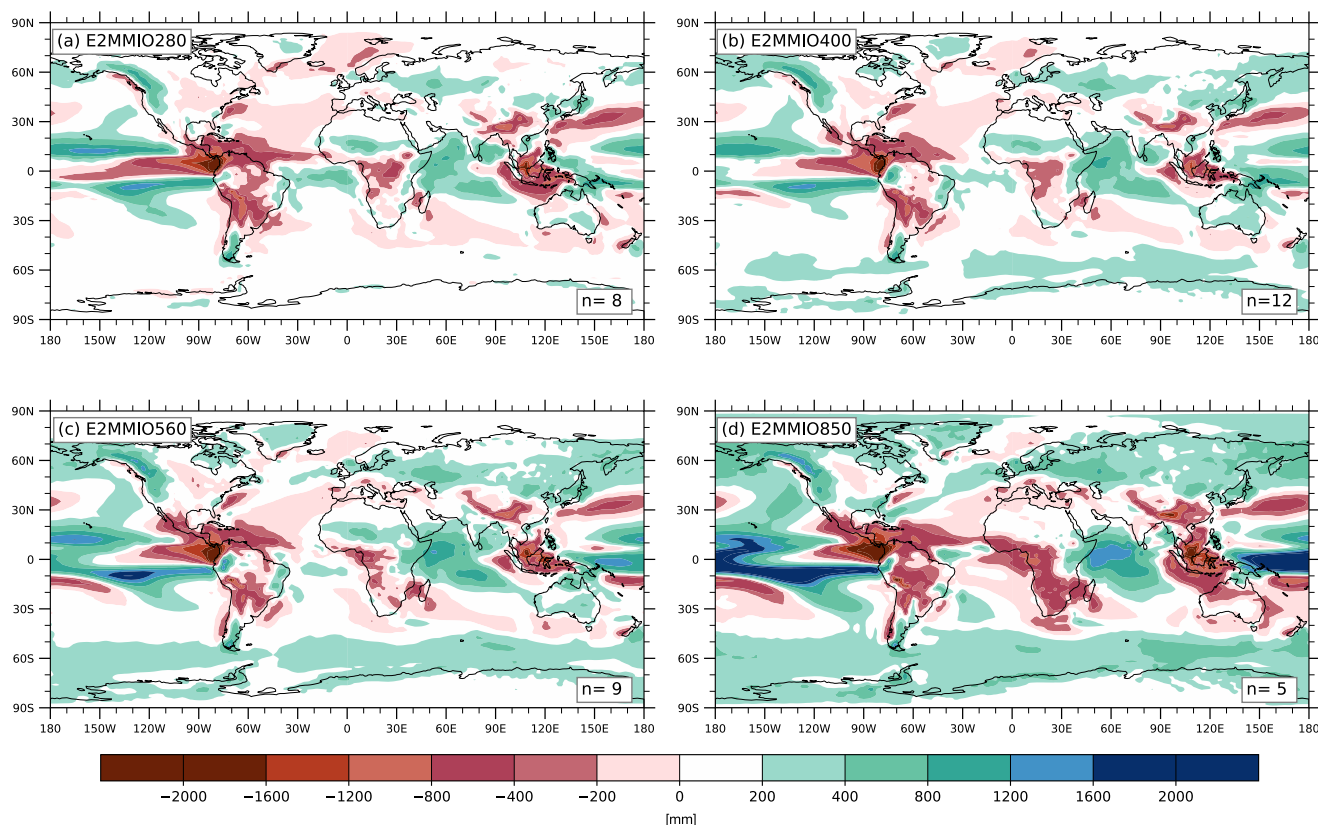
**Figure 3.** Mean annual precipitation (mm) difference between early-to-middle Miocene (E2MMIO) multi-model mean (280, 400, 560, and 850 ppm $CO_2$) and Preindustrial multi-model ensemble mean. The number of models used in the multi-model mean is found in the lower right-hand corner.

are substantially wetter in the NorESM than IPSLCM (Figure S2c in Supporting Information S1), reflecting the low agreement between the M2LMIO 560 ppm simulations (see Section 3.2.3 for details).

### 3.2.2. Precipitation Response to Increased Global Surface Temperature

The strength of the global-mean hydrological cycle under "modern-day" boundary conditions has been shown to scale with surface warming on the order of ~2% $K^{-1}$ (Held & Soden, 2006). The E2MMIO and M2LMIO simulations show a similar change in global mean precipitation per degree change in GMST with increased hydrological sensitivity of 2.06% and 2.27% $K^{-1}$, respectively (Figures 5 and 6b). This indicates that the global mean response of the hydrological cycle to warming is similar in the MioMIP models compared to other CMIP studies (Allan et al., 2020; Held & Soden, 2006; Pendergrass, 2020), albeit forced with different boundary conditions.

We find a positive linear relationship in tropical, mid-latitude, and high-latitude precipitation per degree change in GMST, with an *R*-squared of ~0.60. E2MMIO models show slopes of 2.25%, 1.89%, and 5.59% $K^{-1}$, respectively (Figures 5c, 5e, and 5f). M2LMIO models show a similar linear relationship as the E2MMIO models with slopes of 2.78%, 1.46%, and 6.15% $K^{-1}$, respectively (Figures 6c, 6e, and 6f). The % $K^{-1}$ increase is close to double for the high-latitude regions compared to low-latitude regions due to the combined effects of increased local evaporation and increased poleward moisture transport (Figures S3 and S4 in Supporting Information S1). For both the E2MMIO and M2LMIO models, there are weak linear relationships for the subtropics with slopes of −0.6% and −0.93% $K^{-1}$, respectively (Figures 5d and 6d). These negative slopes follow the thermodynamic expectations over regions where evaporation is greater than precipitation (Held & Soden, 2006). Similar paleoclimate model behavior has been shown in the EoMIP models (Cramwinckel et al., 2023).

To partially explore the drivers of precipitation changes, we provide an analysis of the zonal-mean P-E and moisture transport. The P-E fields for the individual simulations are provided in the Supplementary section (Figures S5 and S6 in Supporting Information S1). The E2MMIO simulations show that the Southern Hemisphere tropics, upper mid-latitude in both Hemispheres and the poles experience much greater P-E rates at warmer temperatures
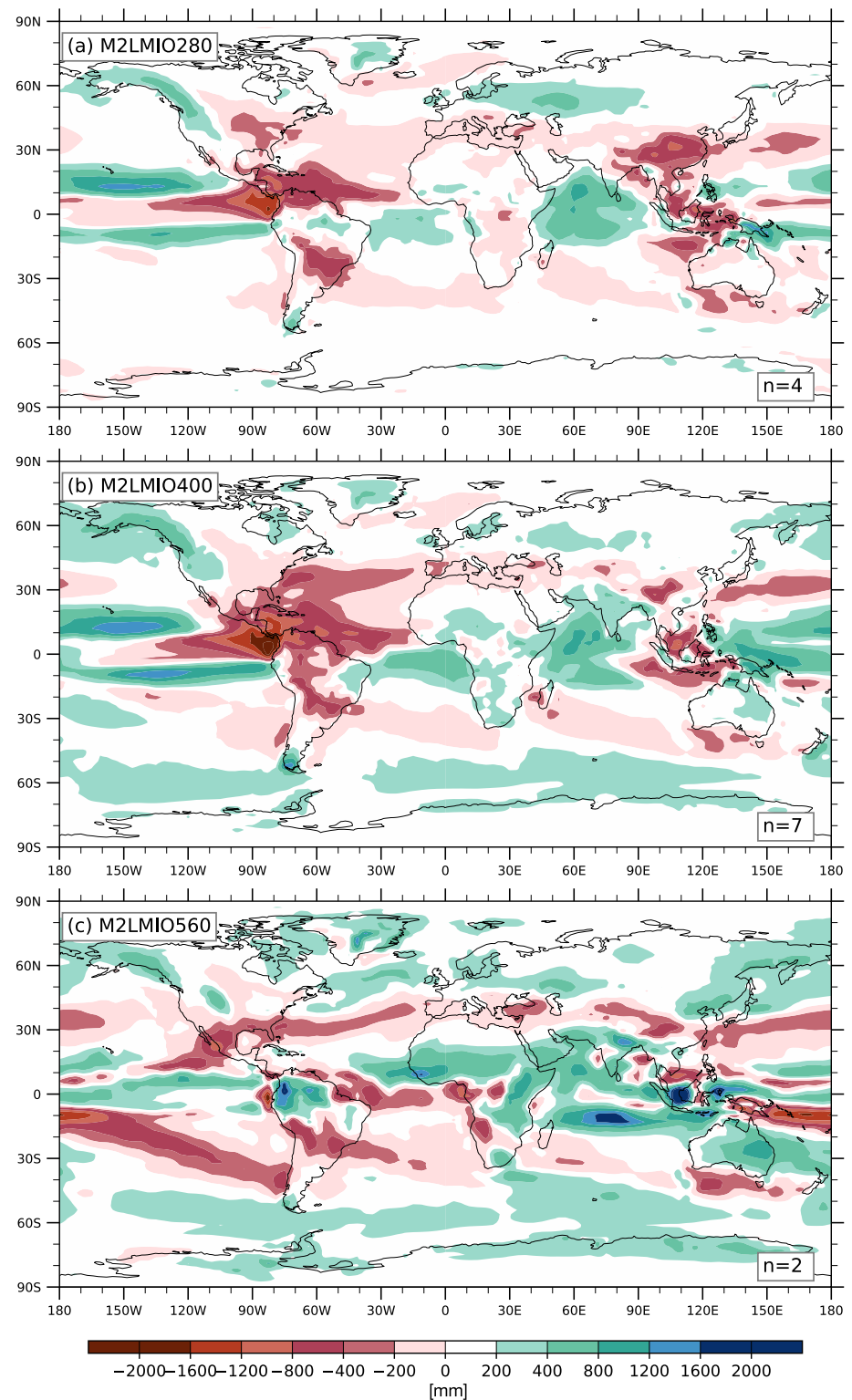
**Figure 4.** Annual mean precipitation (mm) comparison between middle-to-late Miocene (M2LMIO) multi-model mean (280, 400, and 560 ppm $CO_2$) and Preindustrial multi-model mean. The number of models used in the multi-model mean is found in the lower right-hand corner.
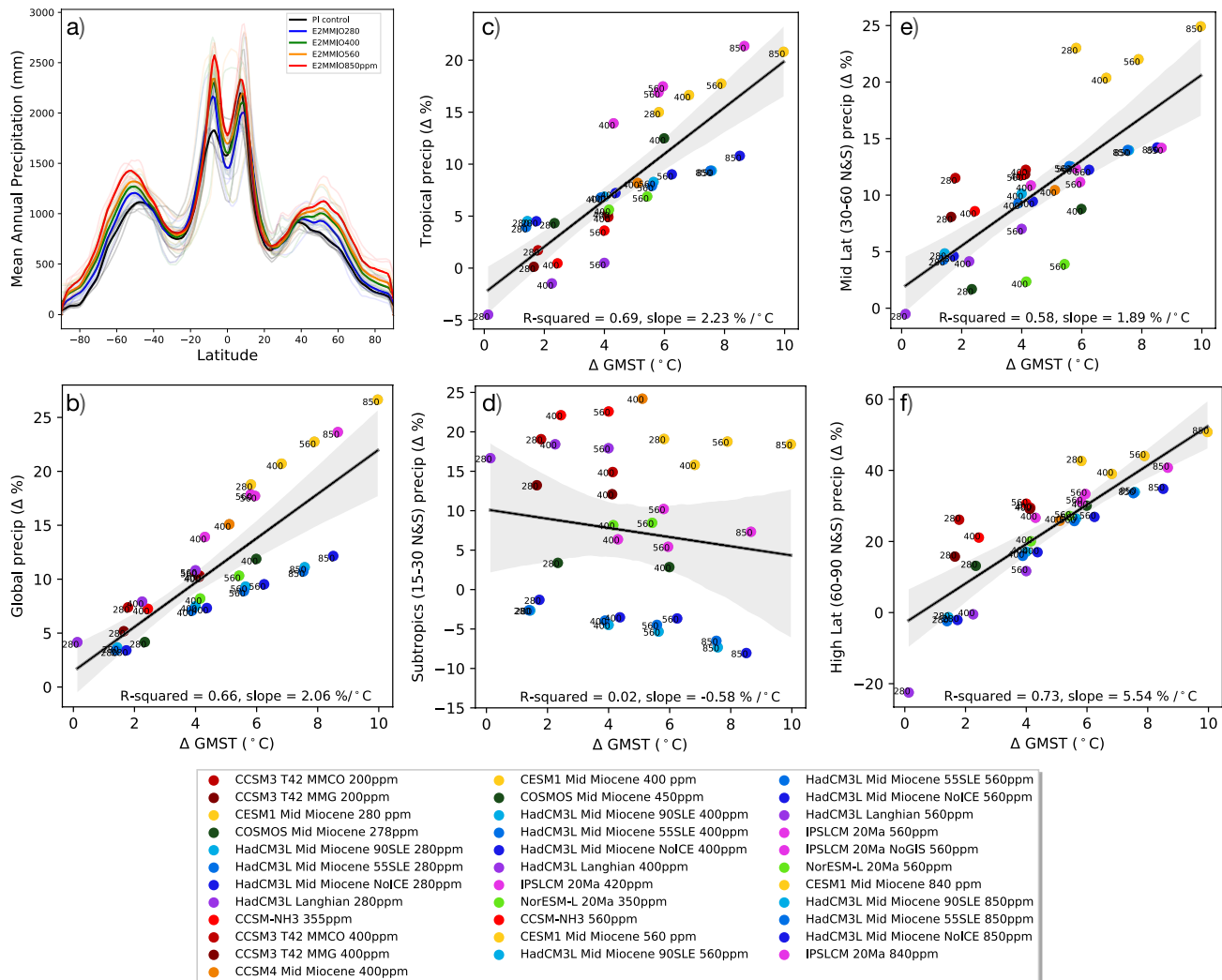
**Figure 5.** Early-to-middle Miocene (E2MMIO) hydrological cycle analysis. (a) Zonal mean annual precipitation of E2MMIO multi-model means (dark colors) and individual models (light colors). Change in precipitation (%) versus global mean change in surface temperature (°C) for (b) global, (c) tropics (15°–15°N and S), (d) subtropics (15°–30°N and S), (e) mid-latitude (30°–60°N and S), and (f) high-latitude (60°–90°N and S). Black line with gray band represents linear regression model with 95% confidence interval.

(Figure 7a). The shift in higher Southern Hemisphere ITCZ precipitation rate (Figure 8a vs. Figure 8d) is due to the enhancement of precipitation over the East Equatorial Pacific and is potentially linked to the tropics experiencing increased local evaporation (Figure S3a in Supporting Information S1). For the mid-latitudes, enhanced local evaporation is the primary factor driving enhanced precipitation with warming across the models, while the influence of moisture divergence changes is mixed. For the high latitudes, both enhanced local evaporation and poleward moisture transport lead to amplified wetting with increased warming (Figure 7b and Figures S3g and S3h in Supporting Information S1). The subtropics experience a systematic increase in evaporation with warming (Figure S3c in Supporting Information S1), however, the increase in moisture divergence and transport toward the pole (Figure 7b and Figure S3d in Supporting Information S1) leads to a decrease in subtropical precipitation in several (but not all) models. An expansion of dry zones toward the mid-latitudes as $CO_2$ concentrations increase is also evident (Figures 7a and 7b). Estimated moisture transport analysis shows E2MMIO simulations experience a systematic enhancement of poleward moisture transport from the subtropics toward the poles as $CO_2$ concentrations increase (Figure 7b), resulting in the occurrence of higher precipitation rate over the high latitudes (Figure S4h in Supporting Information S1).

Unlike the E2MMIO, the M2LMIO simulations do not show a systematic increase in tropical and high-latitude precipitation change with $CO_2$ (Figures 7c and 7d). Enhancement of the Southern Hemisphere branch of the
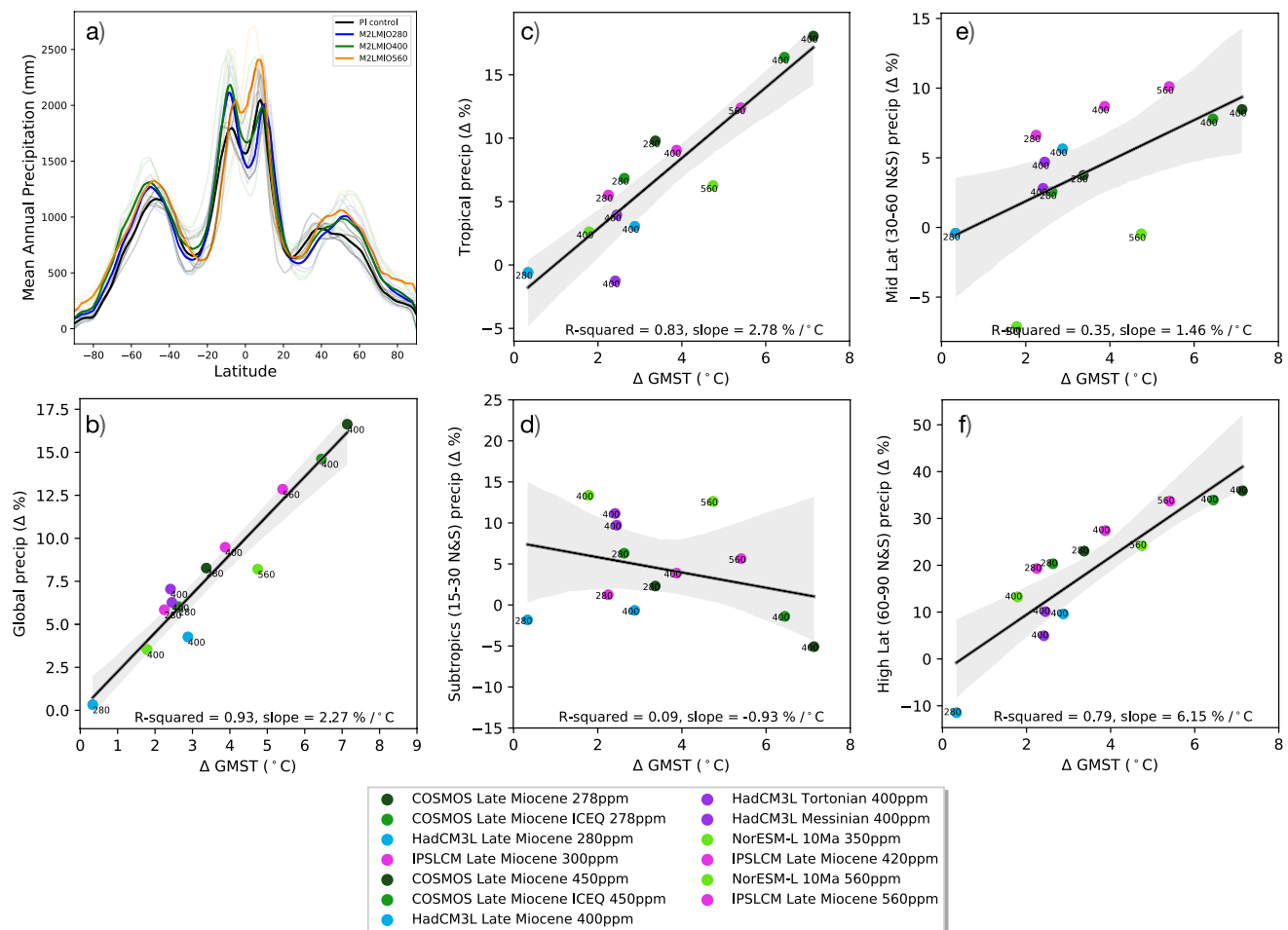
**Figure 6.** Middle-to-late Miocene (M2LMIO) hydrological cycle analysis. (a) Zonal mean annual precipitation of early-to-middle Miocene (E2MMIO) multi-model means (dark colors) and individual models (light colors). Change in precipitation (%) versus global mean change in surface temperature (°C) for (b) global, (c) tropics (15°–15°N and S), (d) subtropics (15°–30°N and S), (e) mid-latitude (30°–60°N and S), and (f) high-latitude (60°–90°N and S). Black line with gray band represents linear regression model with 95% confidence interval.

ITCZ does not increase at higher $CO_2$ (Figure 9). We note that weak model convergence is potentially due to the low number of simulations participating in the 560 ppm multi-model mean. Nonetheless, the clear patterns that emerge are the tropics experiencing increased local evaporation as a source of enhanced ITCZ precipitation (Figure S4a in Supporting Information S1), while the mid- and high-latitude are sourced moisture from both local evaporation and poleward moisture transport (Figure 7d and Figures S4g and S4h in Supporting Information S1).

### 3.2.3. Precipitation Change and Model Agreement

We analyze precipitation change compared to the PI to determine where models show precipitation change (Figures 10 and 11). The E2MMIO 280 ppm simulations (Figures 10a and 11a) represent precipitation changes that are non-$CO_2$ related. A few key regions emerge where the models agree on the impact of Miocene boundary conditions on the hydrological cycle. Over the land, enhanced rainfall with above 80% model agreement occurs over western North America, Northern Africa, Northwest India-Pakistan region, Kazakhstan region, and Antarctica. Drying regions with above 80% model agreement are Central America, central South America, and Central Africa. We suspect the drying over Central Asia-Tibetan region is due to the lower Tibetan-Plateau configuration implemented by the modeling groups. Over the ocean, the models appear to agree on a widening of tropical rainfall into both hemispheres in the eastern equatorial Pacific and into the Southern hemisphere in the South Atlantic and Indian Oceans. The models also agree on decreased precipitation over the eastern equatorial Pacific and part of the North Atlantic. These non-$CO_2$ related changes arise from a combination of the direct response
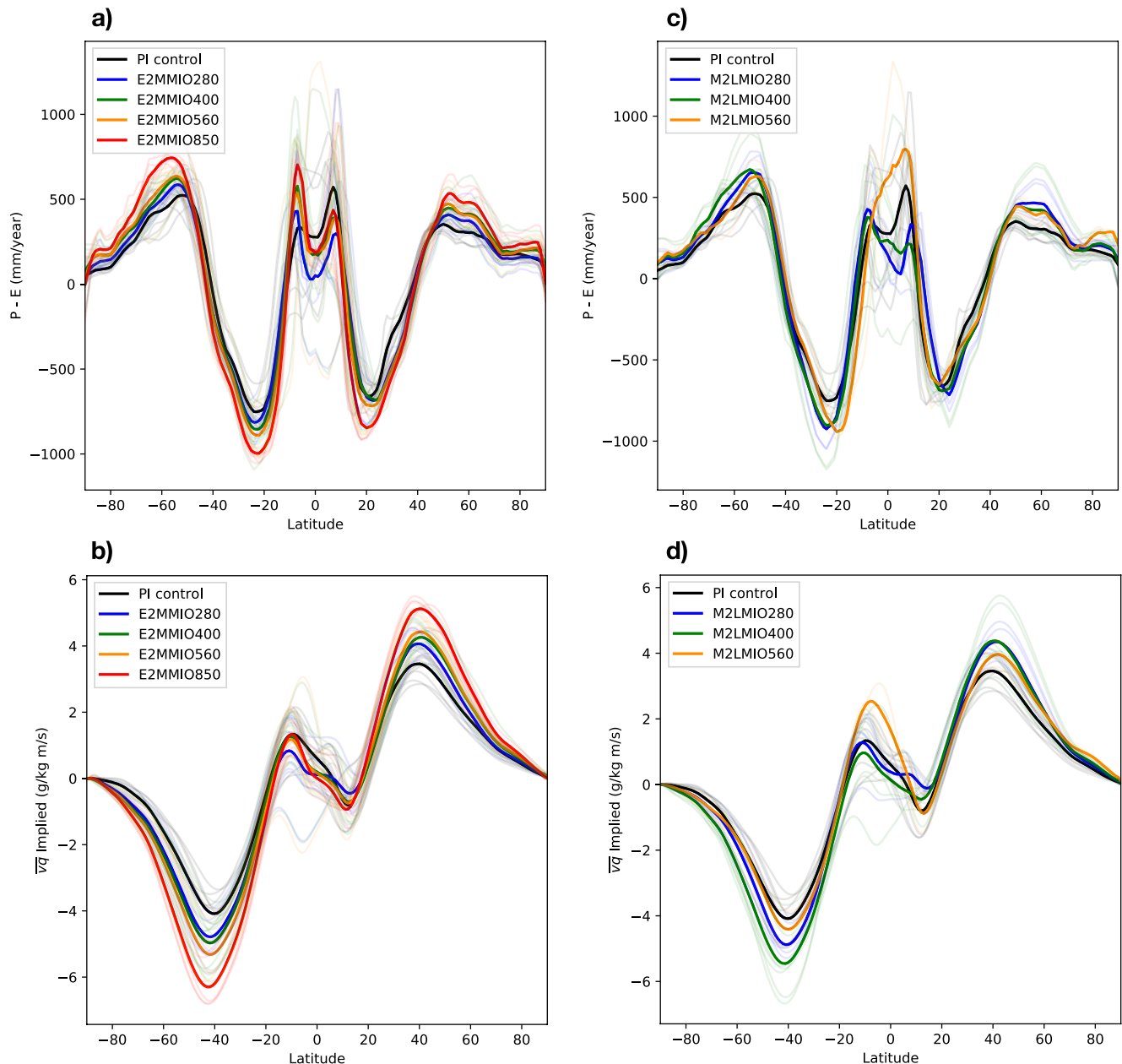
**Figure 7.** Zonal mean hydrological cycle analysis showing P-E (mm yr$^{-1}$) (a and c), and implied zonal mean moisture transport (g kg$^{-1}$ m s$^{-1}$) (b and d) for early-to-middle Miocene (E2MMIO) and middle-to-late Miocene (M2LMIO) multi-model means (dark colors), and individual models (light colors).

to Miocene changes in topography, plate tectonic reconstructions, vegetation, and land ice as well as the indirect response of the hydrological cycle to the global warming induced by non-CO$_2$ boundary conditions (∼2°C, Burls et al., 2021). For example, changes in eastern equatorial Pacific and Central America precipitation are unlikely a response to the warming (Figures 10 and 11), but are likely linked to the open Central American Seaway (Brierley & Fedorov, 2016).

The increased CO$_2$ concentrations in the E2MMIO models (400, 560, and 850 ppm) identify the impact of increasing GMST on the regional hydrological cycle (Figures 10b–10d). Enhanced rainfall with above 80% model agreement under high CO$_2$ concentration emerges, such as in Northern and Southern Hemisphere polar regions. In general, already established dry regions such as Central America, Southern Europe, and Southern Africa get drier. Analysis of M2LMIO simulations identifies similar robust wet and dry patterns as the E2MMIO simulations (Figures 11b and 11c). Regions lacking model agreement are wet regions such as northern South
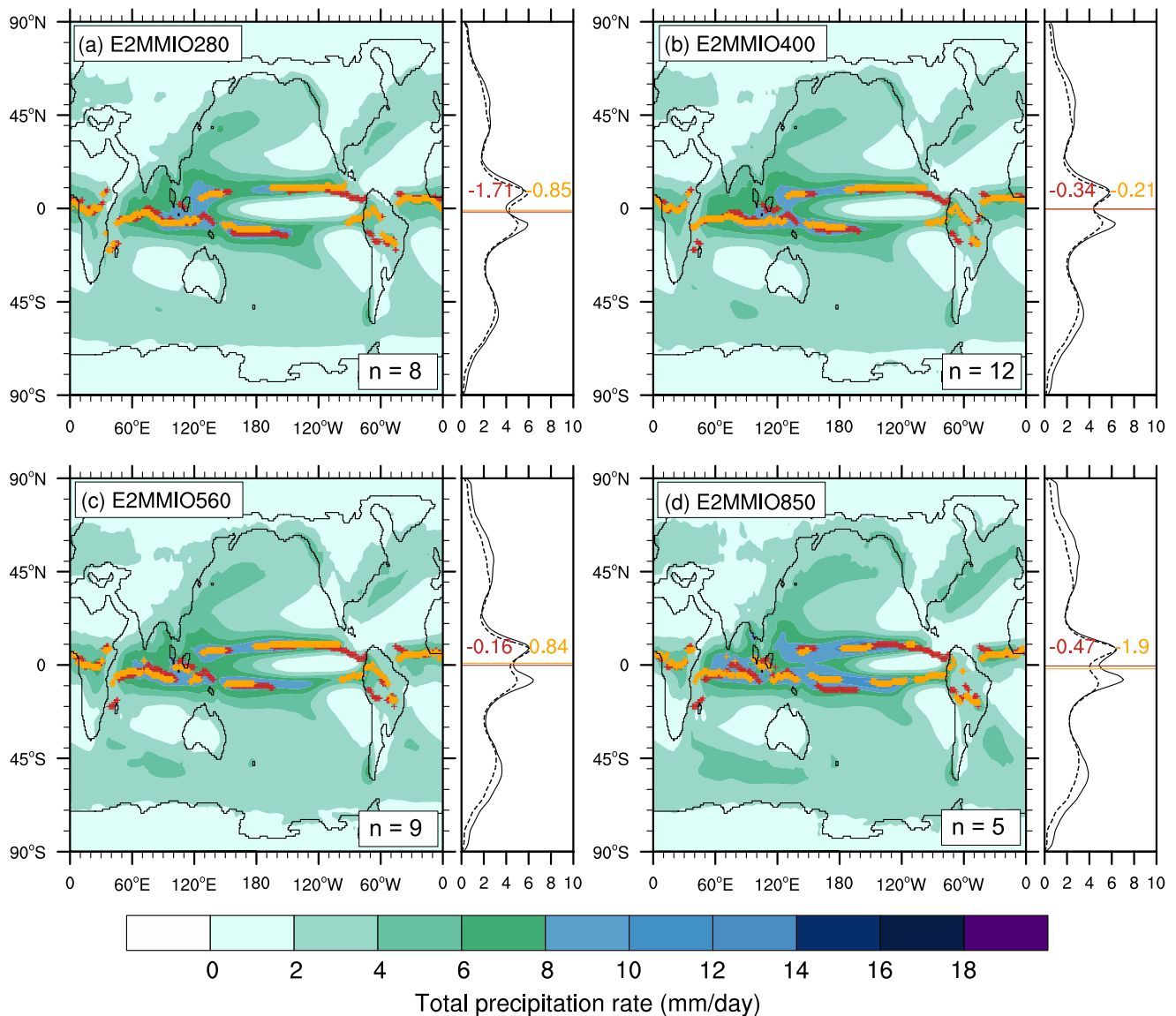
**Figure 8.** The multi-model mean of the annual mean total precipitation rate (mm/day) for the set of early-to-middle Miocene (E2MMIO) experiments with (a) 280 ppm, (b) 400 ppm, (c) 560 ppm, and (d) 850 ppm $CO_2$. Red and orange crosses on the map indicate meridional location of the maximum precipitation in the tropics at each longitude for the Preindustrial and middle Miocene experiments, respectively. Dashed and solid lines represent zonal-mean total precipitation rates for the Preindustrial and middle Miocene experiments, respectively. Red and orange lines indicate the mean latitude of the maximum precipitation for the Preindustrial and middle Miocene experiments, respectively. The number of models used in the multi-model mean is found in the lower right-hand corner.

America, Southern Asia, and Northern Australia, and dry regions such as southwest, central and eastern North America, western Pacific Islands, and most of Southern Australia.

### 3.2.4. Change in Monsoon Precipitation

By using a modern-day monsoon index, we can identify changes in monsoon precipitation distribution during the Miocene. In this section, we primarily focus on the multi-model mean analysis, but individual simulation analysis is found in the Supplementary section (Figures S11 and S12 in Supporting Information S1). Model results suggest the North American Monsoon (NAM) in the E2MMIO occupied a smaller region and was much weaker than the M2LMIO and PI multi-model means (Figures 12a, 12b, 13a, and 13b). We find the low $CO_2$ E2MMIO multi-model mean suggests that non-$CO_2$ boundary conditions such as an open Central American Seaway and lower Central and North American mountain ranges may have lowered NAM precipitation rate and increased subtropical drying due to $CO_2$-induced warming further weakening the NAM precipitation (Figure 12b). The
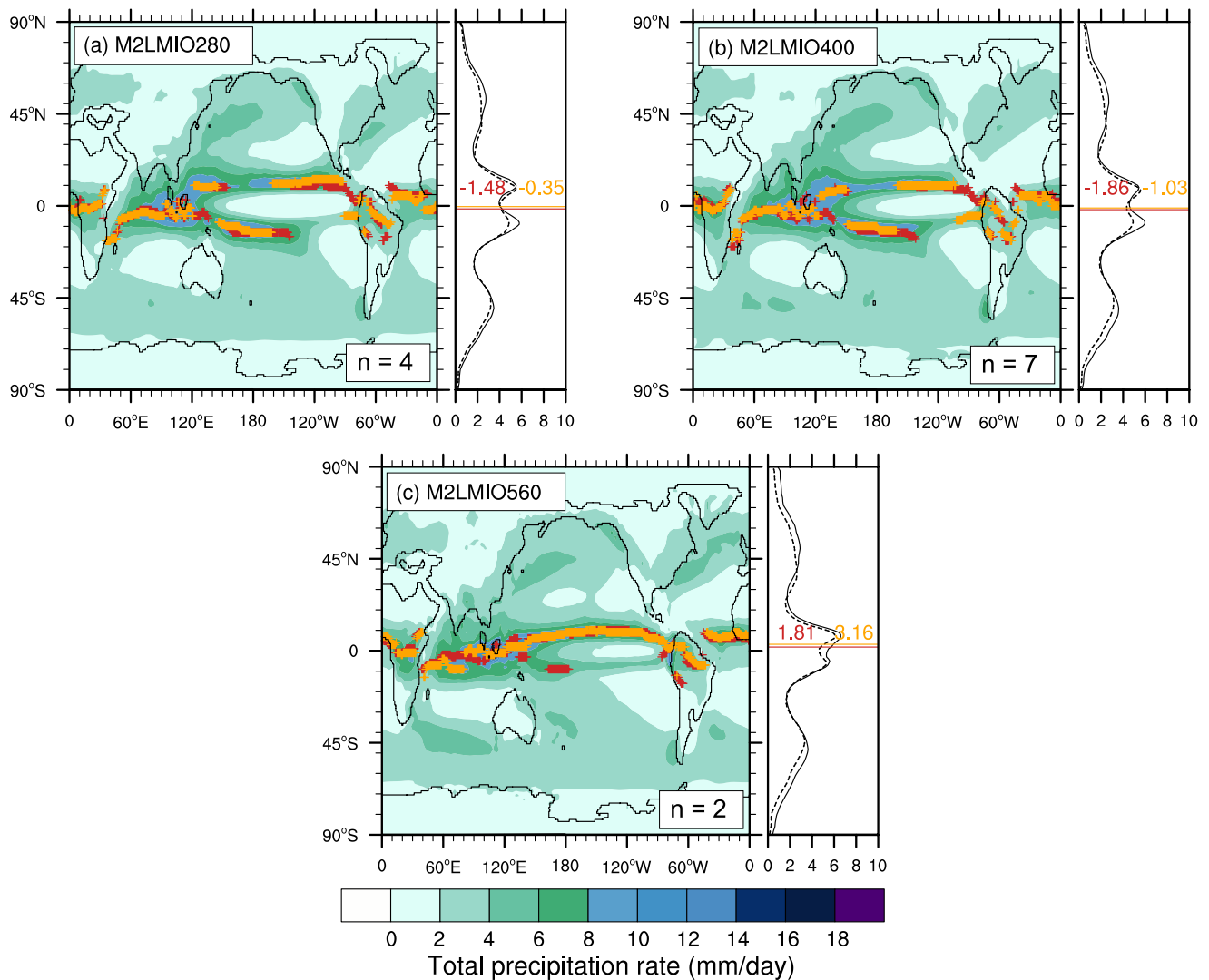
**Figure 9.** The multi-model mean of the annual mean total precipitation rate (mm/day) for the set of early-to-middle Miocene (M2LMIO) experiments with (a) 280 ppm, (b) 400 ppm, and (c) 560 ppm $CO_2$. Red and orange crosses on the map indicate meridional location of the maximum precipitation in the tropics at each longitude for the Preindustrial and late Miocene experiments, respectively. Dashed and solid lines represent zonal-mean total precipitation rate for the Preindustrial and late Miocene experiments, respectively. Red and orange lines indicate the mean latitude of the maximum precipitation for the Preindustrial and late Miocene experiments, respectively. The number of models used in the multi-model mean is found in the lower right-hand corner.

timing and configuration of both the Central American Seaway and Central and North American mountain ranges are an active area of research, which adds uncertainty to our NAM analysis. The region occupied by the South American Monsoon (SAM) stays consistent between the moderate $CO_2$ concentration (400–560 ppm) E2MMIO, M2LMIO, and PI multi-model means, but simulates higher monsoon precipitation rates at 850 ppm (Figures 12a, 12c, 13a, and 13c). The Northern and Southern African Monsoon (NAFM and SAFM) regions also stay roughly consistent under both periods, with the middle-to-late Miocene having slightly higher precipitation than the early-to-middle Miocene (Figures 12a, 12d, 12e, 13a, 13d, and 13e). The regions occupied by the East Asian and Indo-Asian Monsoons (EAM and IAM) remained unaltered under both periods, while their monthly precipitation magnitude progressively increased with higher $CO_2$ concentrations (Figures 12a, 12f, 12g, 13a, 13f, and 13g). The region occupied by the early-to-middle and middle-to-late Miocene Australian monsoon (AM) becomes smaller at higher $CO_2$ concentrations, while monthly precipitation magnitude becomes less seasonal with higher $CO_2$ concentrations (Figures 12a, 12h, 13a, and 13h).

Our results also suggest that models disagree on the sign of change for various monsoon regions (Figures S7 and S8 in Supporting Information S1). For example, a decrease in NAM summer precipitation rate with increasing
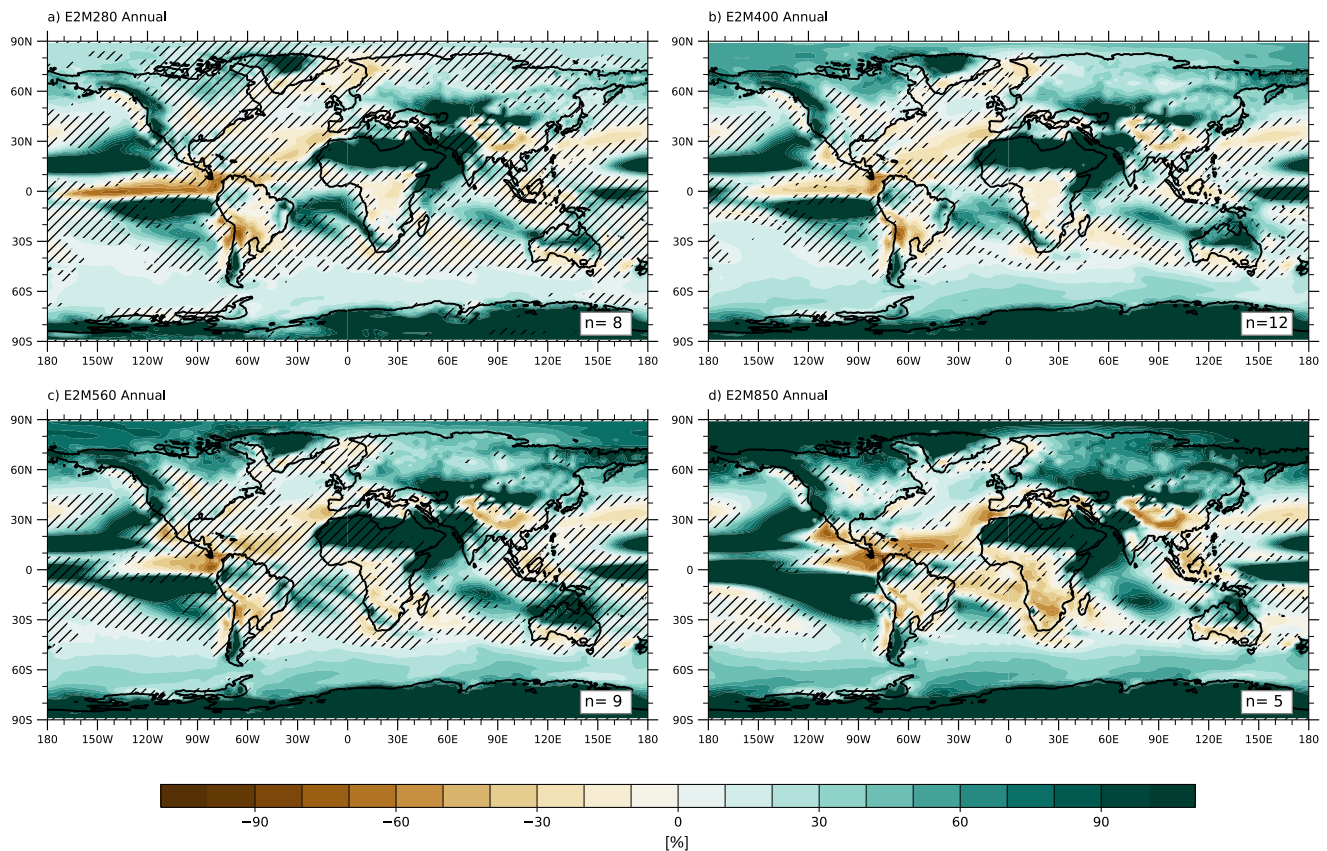
**Figure 10.** Early-to-middle Miocene percent change of annual precipitation compared to preindustrial cases. Hatch marks indicate regions of disagreement (below 80%) between early-to-middle Miocene (E2MMIO) simulations. The lower right corner shows the number of models per ensemble.

$CO_2$ concentrations suggests a weaker monsoon circulation than modern-day (Figures 12b and 13b), however, the model agreement is low (Figures S7 and S8 in Supporting Information S1) and suggests large uncertainty in hydroclimate change. We find that using a modern-day monsoon index on the NAM shrinks the region of interest, which tends to decrease precipitation change (e.g., Figures 12a and 10). Although we find weaker NAM, this does not suggest that western North America was drier during the Miocene. Instead, the multi-model mean suggests a reduced occurrence of monsoon seasonal precipitation. Changes in SAM precipitation between multi-model means also have low agreement and suggest non-$CO_2$ forcings such as topography and vegetation input could be playing a role. The IAM for the E2MMIO multi-model means also shows low agreements between $CO_2$ concentrations until the 850 ppm cases (Figure S7e in Supporting Information S1). Lastly, the AM also has a low model agreement with E2MMIO and M2LMIO, showing wetter conditions at moderate $CO_2$ concentrations but dries at 850 ppm (Figures S7f and S8f in Supporting Information S1).

### 3.3. Model-Data Comparison

#### 3.3.1. Early-To-Middle Miocene

Globally, our model-data comparison shows that all $CO_2$ configurations of the E2MMIO multi-model mean underestimate MAP relative to the paleobotanical proxy estimates (Figures 14 and 16a). A similar global average dry bias of ~−215 mm and an RMSB of ~330 mm is calculated for the multi-model mean for each $CO_2$ concentration (Table 2). An evaluation of individual E2MMIO models (Table 2) shows that most models yield similar MAP RMSB as the ensemble mean (~330 mm respectively), with NorESM, IPSLCM, and CESM1 yielding the lowest global MAP RMSB (~250 mm) and COSMOS, and CCSM4 yielding the highest MAP RMSB (~400 mm). The largest model-data discrepancies are in Europe, Asia, and Australia (Figures 14e−14h). However, relatively good agreements are found over eastern North America and eastern Asia (Figure 16a). Overwhelmingly, the samples in Asia and Europe suggest E2MMIO multi-model means underestimate MAP. Model-data comparison over topical sites in Central America shows good agreement across all multi-model means. The model-data comparison over
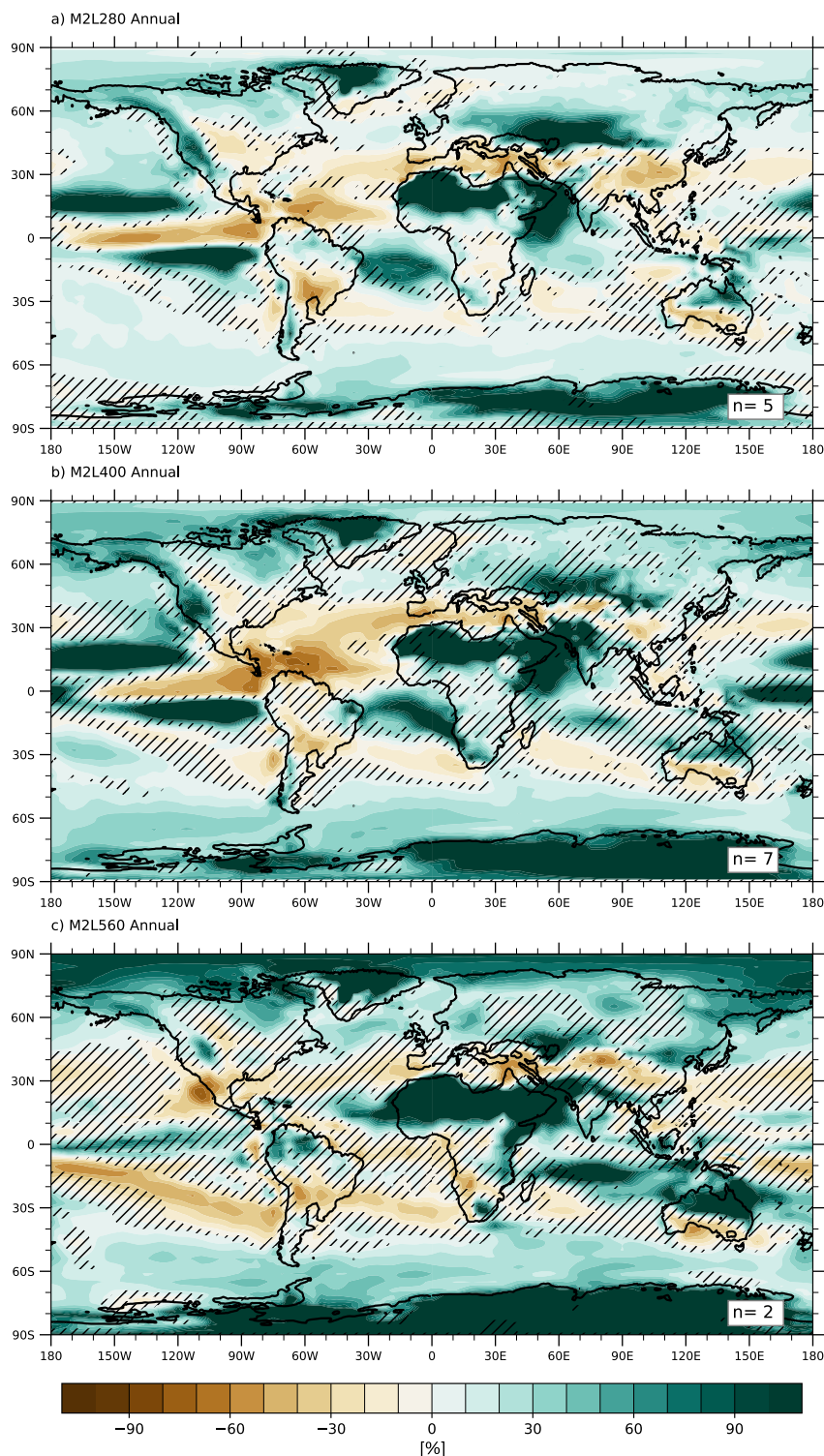
**Figure 11.** Middle-to-late Miocene percent change of annual precipitation compared to preindustrial cases. Hatch marks indicate regions of disagreement (below 80%) between early-to-middle Miocene (M2LMIO) simulations except for M2LMIO 560 ppm simulation where 50% criteria were used. The lower right corner shows the number of models per ensemble.

South America shows the E2MMIO simulations overestimating the sample at ~30°S while underestimating the sample found at 40°S. The South American sample located at ~30°S is at the border between the subtropical dry and mid-latitude wet regions, and the E2MMIO models could be getting the precipitation transition between the
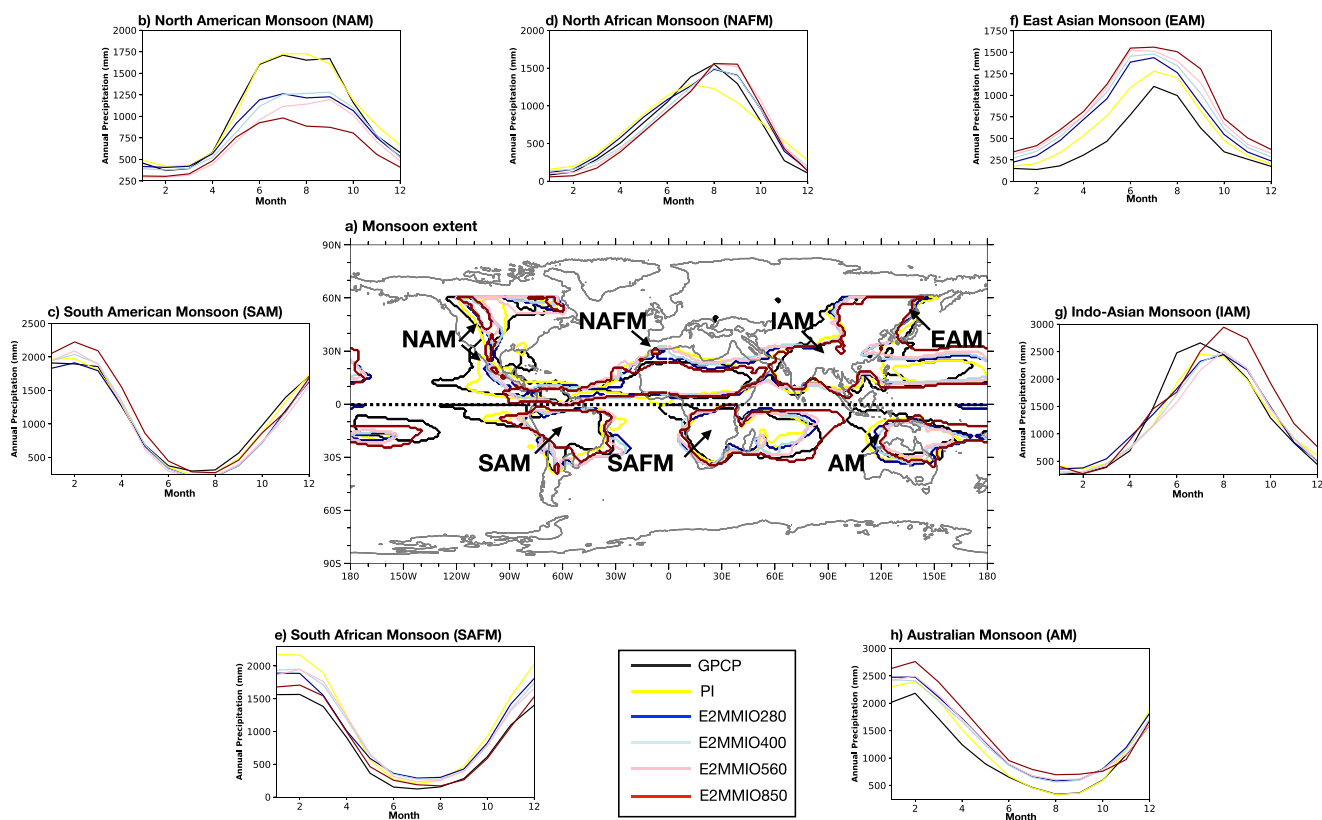
**Figure 12.** Early-to-middle Miocene global monsoon distribution (a). Annual precipitation cycle for regional monsoons: North American (b; NAM), South American (c; SAM), Northern African (d; NAFM), Southern African Monsoon (e; SAFM), East Asian Monsoon (f; EAM), Indo-Asian Monsoon (g; IAM), and Australian Monsoon (h; AM). Experiments show observation, Global Precipitation Climate Project (black), multi-model preindustrial ensemble (yellow), and early-to-middle Miocene multi-model ensembles 280 ppm (dark blue), 400 ppm (light blue), 560 ppm (pink), and 850 ppm (red). Monsoon extent in plot a shows regions where the percentage (>55%) of mean annual precipitation occurring during the extended boreal summer season (MJJAS, Northern Hemisphere) and during the extended austral summer season (NDJFM, Southern Hemisphere) delineated by dotted line over the equator. The regional annual precipitation cycle calculation is based on the regional monsoon extent.

regions incorrectly. The lack of published African MAP samples presents a caveat to this study, encouraging the next iteration of MioMIP to focus on adding more data over the region.

Increasing $CO_2$ concentrations does reduce some regional model-data discrepancies. For example, biases found along 40°–60°N and S, like those found in Northern Eurasia, South America, Australia, and New Zealand, tend to decrease at higher $CO_2$ concentrations, but overall, still underestimate proxy reconstructions. Such improvement is due to the increase in high-latitude precipitation at higher GMST (Figure 10a vs. Figure 10d). Out of the E2MMIO simulations, the 560 ppm multi-model mean has the best agreement with the proxies, with the 560 ppm NorESM and CESM1 simulations having the lowest RMSB (Table 2).

### 3.3.2. Middle-To-Late Miocene

Overall, the 560 ppm M2LMIO simulations have the best agreement with the proxies, with the 560 ppm multi-model mean having the lowest mean bias and RMSB of ∼–98 and ∼246 mm, respectively (Table 2, Figure 16a, and Figure S13 in Supporting Information S1). Similarly to the E2MMIO multi-model means, the M2LMIO multi-model means exhibit the largest biases over Europe, southern Asia, and southern Australia. There is relatively good agreement with samples found over southwest North America, northern Eurasia, Pacific Islands, and East Asia (Figure 15). In general, increasing $CO_2$ concentrations reduces some of the model-data discrepancies in both multi-model mean and individual models (Figure 17b). For example, the model-data agreement increases at higher $CO_2$ concentrations, agreeing with relatively wetter than modern-day conditions over Europe (Figures 15 and 17a). Over central and east Asia, both 280 and 400 ppm multi-model mean underestimate MAP, while the 560 ppm shows better agreement. Samples found over India are underestimated by both 280 and 400 ppm multi-model ensembles but can capture wet conditions over southeast Asia. Only at 560 ppm does
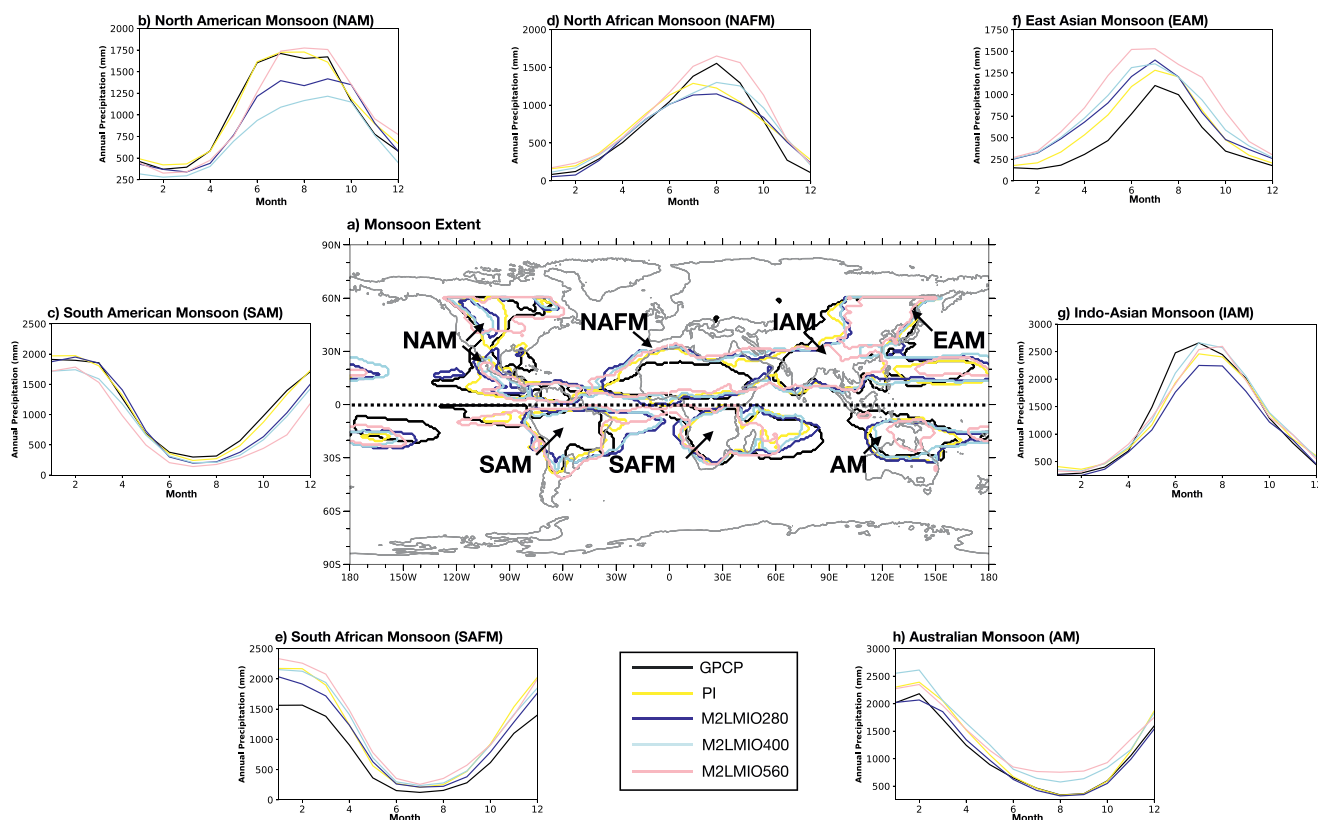
**Figure 13.** Middle-to-late global monsoon distribution (a). Annual precipitation cycle for regional monsoons: North American Monsoon (b; NAM), South American Monsoon (c; SAM), Northern African Monsoon (d; NAFM), Southern African Monsoon (e; SAFM), East Asian Monsoon (f; EAM), Indo-Asian Monsoon (g; IAM), and Australian Monsoon (h; AM). Experiments show observation, Global Precipitation Climate Project (black), multi-model preindustrial ensemble (yellow), and middle-to-early Miocene multi-model ensembles 280 ppm (dark blue), 400 ppm (light blue), and 560 ppm (pink). Monsoon extent in plot shows regions where the percentage (>55%) of mean annual precipitation occurring during the extended boreal summer season (MJJAS, Northern Hemisphere) and during the extended austral summer season (NDJFM, Southern Hemisphere) delineated by dotted line over the equator. The regional annual precipitation cycle calculation is based on the regional monsoon extent.

model-data agreement over India improve, representing wetter Indo-Asia than modern-day. The single sample found over southern Australia is consistently underestimated by all multi-model ensembles, suggesting that the M2LMIO models tend to have a dry bias over southern Australia (Figure 17g).

### 3.3.3. Potential Sources of Model-Data Discrepancy

We extend our model-data comparison by comparing simulated regional and seasonal precipitation fields against reconstructed MAP. Regional RMSB is subject to change when given a smaller domain than the ones presented (Figures 16a and 17a). However, setting such domains is subject to further debate, thus, we opted for a more encompassing set of regions. Our analyses indicate that the multi-model mean can yield improved RMSB when seasonal precipitation is accounted for (Figures 16 and 17). E2MMIO model-data comparison shows better agreement over Europe when accounting for extended boreal winter precipitation but worsens when accounting for extended boreal summer months (Figures 16e and 17e). Over northern Eurasia and eastern Asia, model-data comparison improves when accounting for extended boreal summer months and worsens under extended boreal winter months (Figures 16f and 17f). However, the model-data comparison over North and South America and Australia did not improve under different seasons (Figures 16c, 16d, 16g, 17c, 17d, and 17g). For the M2LMIO ensemble, using model seasonality over various regions impacts model-data agreement. For instance, samples found in Europe substantially improved during extended boreal winter months (Figure 16e), and samples over Eurasia also improved during extended boreal summer months (Figure 16f). We found no improvements over North and South America and Australia under differing seasonal precipitation.

We find the use of different paleotopography by the different modeling groups represents uncertainty in our analysis and is most likely impacting MAP bias. To understand the role of paleotopography, we isolate the
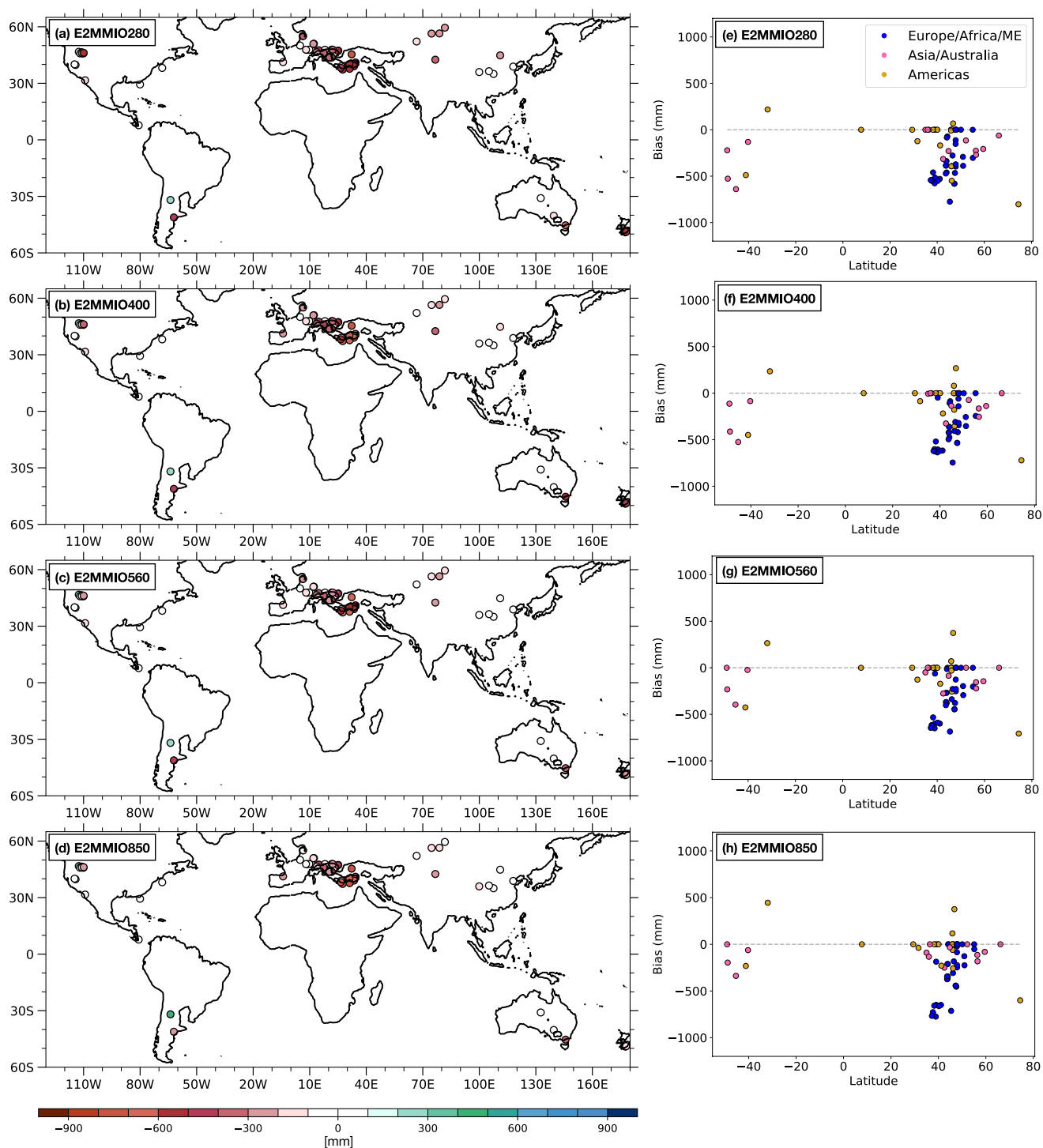
**Figure 14.** Early-to-middle Miocene model-data mean annual precipitation (MAP) bias spatial analysis (a–d) and MAP bias plotted as a function of latitude (e–h). Experiments show multi-model ensemble 280 ppm (a, e), 400 ppm (b, f), 560 ppm (c, g), and 850 ppm (d, h).

280 ppm E2MMIO simulations, which minimizes the impact of $CO_2$ on the hydrological cycle and allows us to focus on the impact of high topography. For example, over eastern Asia, simulations with a high Tibetan Plateau (Figures 18a–18d) simulate higher East Asian Monsoon rainfall than those without or lower Tibetan Plateau (Figures 18e–18h), which substantially improves model-data agreement. Similar improvements occur over the European Alps and the North American Rockies (Figures S19 and S20 in Supporting Information S1).

**Table 2**
*Early-To-Middle and Late-To-Middle Miocene Mean Annual Precipitation (mm), Mean Bias, and Root Mean Squared Bias Analysis*

| | 280 MAP | 280 Bias | 280 RMSB | 400 MAP | 400 Bias | 400 RMSB | 560 MAP | 560 Bias | 560 RMSB | 850 MAP | 850 Bias | 850 RMSB |
|---|---|---|---|---|---|---|---|---|---|---|---|---|
| *E2MMIO models* | | | | | | | | | | | | |
| CCSM3-NH3 | | | | 1040.8 | −245.2 | 351.2 | 1074.2 | −238.5 | 348.5 | | | |
| CCSM3 MMCO | 1042.1 | −230.7 | 333.5 | 1094.4 | −228.0 | 346.4 | | | | | | |
| CCSM3 MMG | 1043.3 | −223.4 | 327.9 | 1093.4 | −227.5 | 345.5 | | | | | | |
| CCSM4 | | | | 1209.4 | −219.5 | 370.3 | | | | | | |
| CESM1 | 1258.7 | −125.4 | 226.9 | 1279.1 | −168.2 | 307.8 | 1300.7 | −160.9 | 298.9 | 1342.0 | −153.5 | 306.3 |
| COSMOS | 1037.6 | −417.7 | 565.6 | 1114.4 | −388.3 | 555.1 | | | | | | |
| HadCM3L 90SLE | 1078.5 | −233.5 | 344.9 | 1118.2 | −223.5 | 341.7 | 1137.2 | −226.6 | 349.7 | 1155.9 | −224.9 | 348.5 |
| HadCM3L 55SLE | 1075.6 | −238.3 | 351.3 | 1113.9 | −224.3 | 338 | 1132.9 | −222.5 | 341.7 | 1151.8 | −224.3 | 352.4 |
| HadCM3L NoICE | 1075.7 | −235.3 | 346.3 | 1116.5 | −221.4 | 332.4 | 1139.4 | −215.2 | 333.9 | 1166.7 | −222.8 | 349.5 |
| HadCM3L Langhian | 1088.9 | −236.8 | 364.7 | 1128.2 | −236.6 | 357.9 | 1158.5 | −252.2 | 364.9 | | | |
| IPSLCM | | | | 1162.1 | −102.2 | 294.1 | 1202.4 | −117.5 | 322.3 | 1261.3 | −171.1 | 345 |
| IPSLCM NoGIS | | | | | | | 1200.9 | −146.9 | 337.5 | | | |
| NorESM | | | | 1082.7 | −214.2 | 293.1 | 1103.9 | −214.5 | 295 | | | |
| Ensemble | 1087.6 | −247.7 | 344.1 | 1129.5 | −229.7 | 337.2 | 1161.1 | −194.2 | 308.2 | 1215.6 | −190.7 | 323.7 |
| *M2LMIO models* | | | | | | | | | | | | |
| COSMOS | 1078.5 | −301.5 | 464.5 | 1161.7 | −291.1 | 485.9 | | | | | | |
| COSMOS ICEQ | 1056.1 | −292.2 | 440.5 | 1141.6 | −286.9 | 474 | | | | | | |
| HadCM3L | 10,437 | −297.0 | 535.1 | 1084.7 | −246.4 | 480.3 | | | | | | |
| HadCM3L Tortonian | | | | 1119.1 | −109.9 | 426.4 | | | | | | |
| HadCM3L Messinian | | | | 1110.9 | −129.4 | 312.3 | | | | | | |
| NorESM | | | | 1036.0 | −91.4 | 351.8 | 1082.8 | −48.9 | 358.3 | | | |
| IPSLCM | 1079.8 | −207.0 | 499.0 | 1116.9 | −201.9 | 497.9 | 1151.3 | −203.9 | 499.8 | | | |
| Ensemble | 1064.5 | −259.4 | 459.1 | 1110.1 | −178.7 | 338.1 | 1117.0 | −98.1 | 246.5 | | | |

*Note.* MAP, mean annual precipitation; RMSB, root-mean-squared error of the bias.

## 4. Discussion

The MioMIP1 models were configured with a range of plausible $CO_2$ concentrations. Comparison between simulations with $1 \times$ PI $CO_2$ concentrations suggests that non-$CO_2$ boundary conditions increase global MAP by ~50 mm (Table 2), with much larger differences in regional precipitation (Figures 3a and 4a). We found that MioMIP models show intensification of the hydrological cycle as we increase $CO_2$ concentrations with a hydrological sensitivity of ~2% per degree of warming. Similar intensification of the hydrological cycles has been shown for CMIP (Pendergrass, 2020), EoMIP (Carmichael et al., 2016; Cramwinckel et al., 2023), and PlioMIP (Han et al., 2021) studies. In comparison, the MioMIP of opportunity has a slightly weaker hydrological sensitivity than the CMIP5 and CMIP6 models, which, on average, have ~2.6 and ~2.5% K$^{-1}$ respectively (Pendergrass, 2020). More recent EoMIP estimates (~2.4% K$^{-1}$; Cramwinckel et al., 2023) also show higher hydrological sensitivity than MioMIP1 models. The lower MioMIP hydrological sensitivity is likely due to the incorporation of legacy model configurations, which compared closer to models found in Held and Soden (2006), and overall had a lower climate sensitivity (Zhu et al., 2020). We expect the next version of MioMIP, which will primarily use model versions closer to CMIP5 and CMIP6, to have higher hydrological sensitivity (Pendergrass, 2020).

The ITCZ and global monsoon distribution between the modern-day and the Miocene generally occupied the same areas, with the extent and intensity varying slightly. For instance, the ITCZ in the MioMIP1 maintains similar Northern Hemisphere precipitation rates as the PI multi-model mean, but there is a progressive increase in Southern Hemisphere ITCZ (0°–10°S) precipitation rates at higher $CO_2$ concentrations. The strengthening of
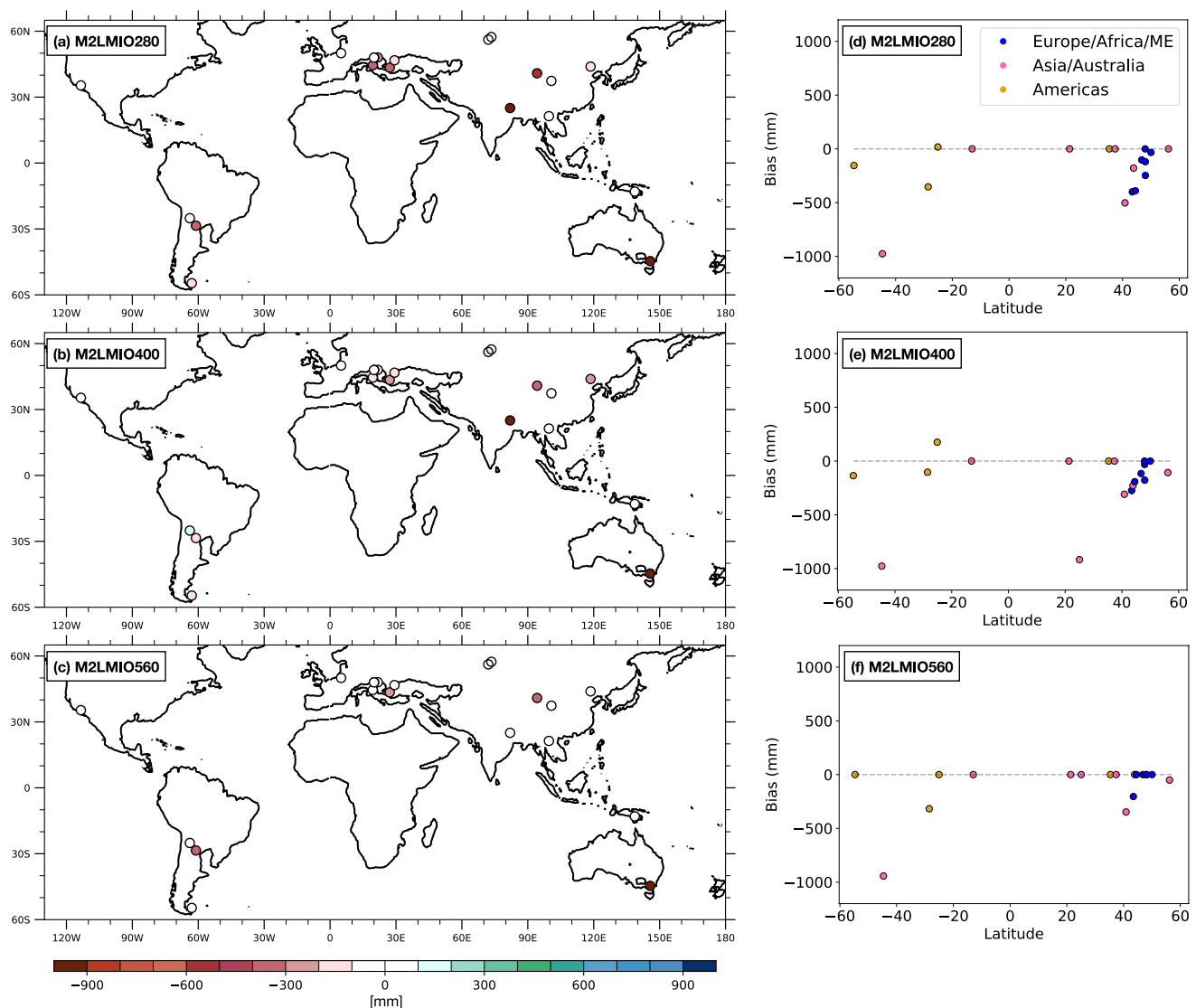
**Figure 15.** Middle-to-late Miocene model-data mean annual precipitation (MAP) bias analysis (a–c) and MAP bias plotted as a function of latitude (d–f). Experiments show multi-model ensemble 280 ppm (a, d), 400 ppm (b, e), and 560 ppm (c, f).

the Southern Hemisphere ITCZ in response to warming is in contrast to the weakening ITCZ in future projections (Byrne et al., 2018), but is similar to the strengthening found in EoMIP studies (Cramwinckel et al., 2023). The NAM was narrower and weaker than modern-day in the E2MMIO simulations with higher $CO_2$ concentrations. The NAM weakening is in accordance with recent high-resolution future warming projections for the region (Pascale et al., 2017). However, early-to-middle Miocene proxies, as well as supporting information from the Pliocene (Bhattacharya et al., 2022), indicate wetter NAM conditions than the MioMIP models and highlight potential divergence from the expected subtropical drying and weakening NAM circulation (Burls & Fedorov, 2017). The simulated changes in the SAM, EAM, and AM intensity are in accordance with monsoon strengthening with increased $CO_2$ concentrations (Douville et al., 2021; Geen et al., 2020). Weak changes to the IAM and NAFM are simulated by the multi-model means yet exhibit a substantial increase in summer precipitation rates at $CO_2$ concentrations above 800 ppm. The abrupt change in IAM and NAFM precipitation intensity at much higher $CO_2$ concentrations could reflect a tipping point in these monsoon regions. However, we lack early-to-middle Miocene MAP records over Indo-Asia and northern Africa, which does not allow us to verify the accuracy of model behavior during this period. Conclusions on SAFM being weaker than today during the warmer period of the Miocene are also uncertain since most multi-model means fall between PI and GPCP precipitation rates. Further robust
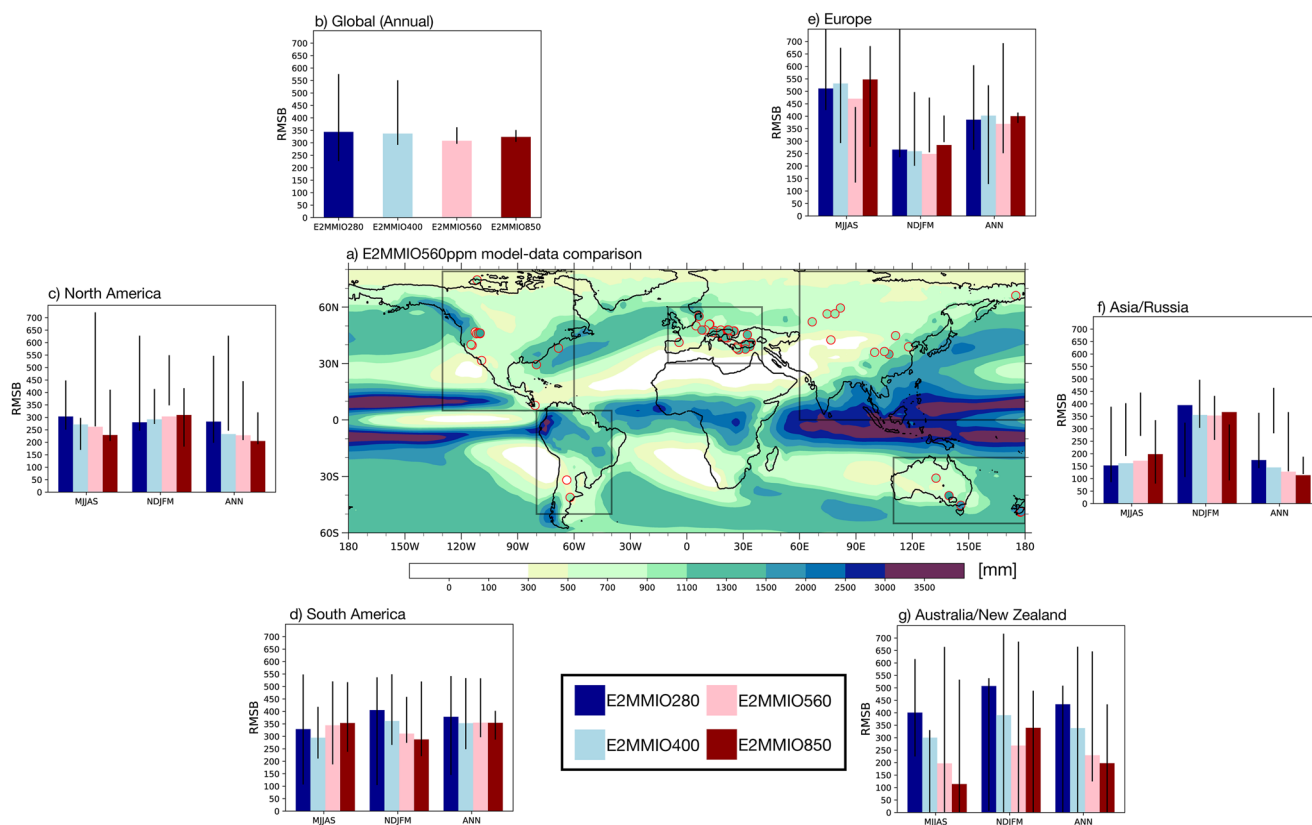
**Figure 16.** Early-to-middle Miocene model-data mean annual precipitation (MAP) root-mean-squared error of the bias (RMSB) comparison. Experiments show multi-model ensemble of 280 ppm in dark blue, 400 ppm in light blue, 560 ppm in pink, and 850 ppm in dark red. Early-to-middle Miocene 560 ppm ensemble MAP overlayed with paleobotanical proxy MAP (a). Spatial analysis shows global (b) and regional analysis of North America (c), South America (d), Europe (e), Eurasia (f), and Australia (g). Temporal analysis shows annual RMSB and breakdown of seasonal RMSB showing extended boreal summer: May, June, July, August, and September, and extended austral summer: November, December, January, February, and March compared to paleobotanical-derived MAP. Black lines show the minimum and the maximum RMSB calculated from individual models.

conclusions on regional monsoon circulations require seasonal analysis of proxy samples, which we lack in our study but should be pursued further as more proxy data becomes available.

Similar to Herold et al. (2010), we found most of the MioMIP1 models underestimate proxy-derived MAP, especially for proxies found in the mid- to high-latitude. The early-to-middle Miocene MAP bias extends across all $CO_2$ concentrations receiving similar bias and RMSB values and suggesting that the models may not be resolving (1) key processes driving the hydrological cycle response to elevated $CO_2$ concentrations and/or (2) the role of other Miocene boundary conditions besides $CO_2$. As demonstrated by Herold et al. (2010), a prescribed weaker temperature gradient results in better model-data agreement. Thus, the inability of early-to-middle Miocene models to simulate the degree of polar amplified warming and reduced equator-to-pole temperature gradients (Burls et al., 2021) is a potential reason for the MAP model-data discrepancy. In support of this, previous work from EoMIP (Carmichael et al., 2016; Cramwinckel et al., 2023) also shows climate models underestimating paleobotanical-derived MAP and highlights the role of accurately capturing equator-to-pole temperature gradients and the need for a more refined model-data analysis through additional modeling and proxy sampling.

The connection between model-predicted precipitation change and proxy signal illustrates if the modeled hydrological response toward higher $CO_2$ concentrations is in agreement with proxies. We found that the few samples close to the high-latitudes (>50°N and S) have better model-data agreement at higher $CO_2$ concentrations, suggesting the increased change in precipitation at high latitudes is consistent with the proxies. Additionally, the tropics also show positive precipitation change and depict higher rainfall rates at higher $CO_2$. The single tropical early-to-middle Miocene sample shows good model-data agreement regardless of the prescribed $CO_2$ concentrations (Figure 14), suggesting that even at 850 ppm, E2MMIO models fall within the range of uncertainty for
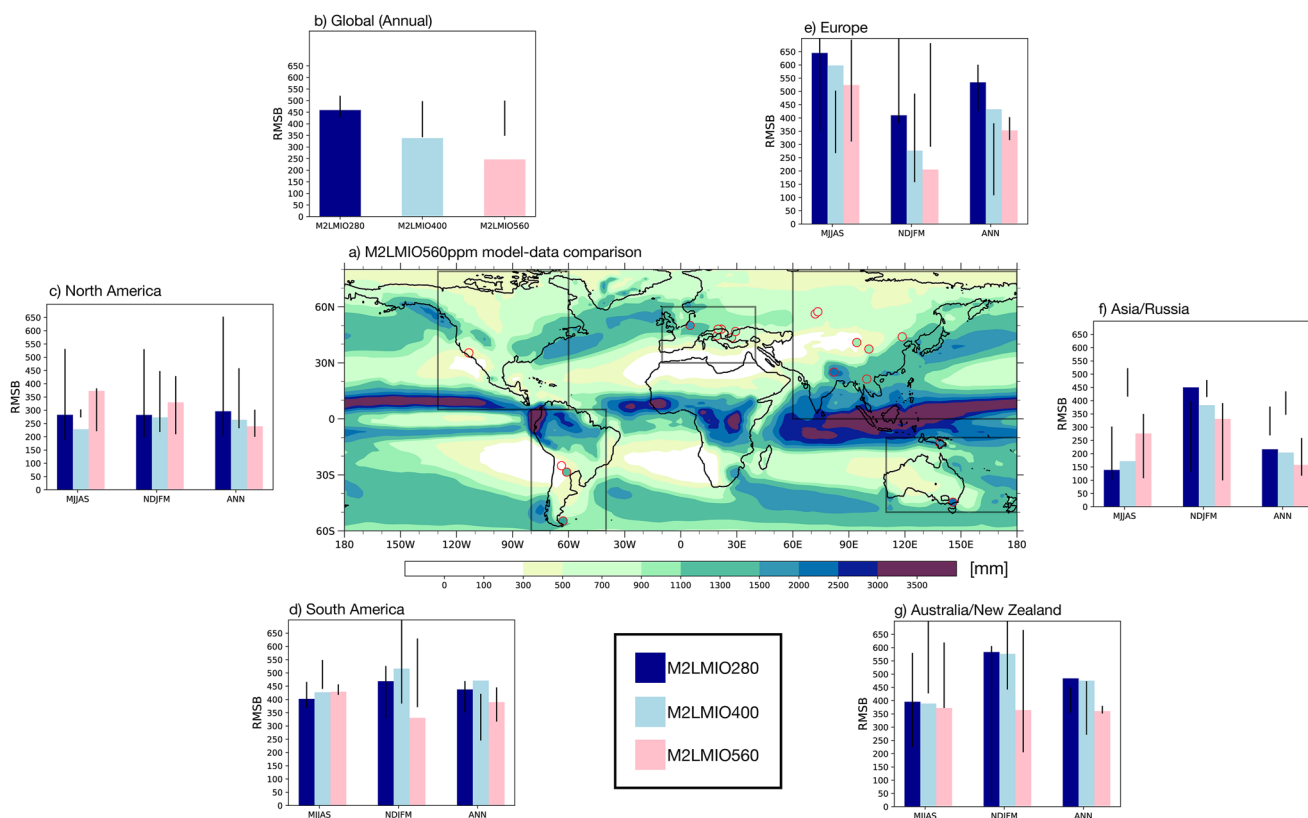
**Figure 17.** Middle-to-late Miocene model-data mean annual precipitation (MAP) RMSE comparison. Experiments show multi-model ensemble 280 ppm in dark blue, 400 ppm in light blue, and 560 ppm in pink. Middle-to-late Miocene 560 ppm ensemble MAP overlayed with paleobotanical proxy MAP (a). Spatial analysis shows global (b) and regional analysis of North America (c), South America (d), Europe (e), Eurasia (f), and Australia (g). Temporal analysis shows annual RMSE and breakdown of seasonal RMSE showing extended boreal summer: May, June, July, August, and September, and extended austral summer: November, December, January, February, and March compared to paleobotanical-derived MAP.

the tropical paleobotanical record. Recent EoMIP study suggest more up-to-date versions of climate models generally overestimate proxy-derived tropical precipitation (Cramwinckel et al., 2023), and the small sample of reconstructed tropical precipitation estimates adds uncertainty to the simulated tropical precipitation. There are also regions where inter-model and model-data agreements are low. In particular, both E2MMIO and M2LMIO multi-model means show drying signals over much of Europe, especially at higher $CO_2$ concentrations, and yet proxy reconstruction describes a much wetter environment. The subtropics (15°–30°N and S) and the African continent both have the lowest model agreement and also lack samples to compare with, therefore lowering our confidence in model behavior over both regions.

Further analysis with more rigorous methodologies should be pursued in future MioMIP iterations. A more comprehensive monsoon analysis using moist static energy can further help explain changes in regional monsoon distribution beyond simplified modern-day-based monsoon indices. The Neogene warm climates have been hypothesized to induce a reduction in the tropical Pacific east-west SST difference similar to the reduction that occurs intermittently during modern-day El Niño events. Future analysis should investigate the occurrence of this in both the proxy data and the models and its implication on the hydrological cycle (e.g., Burls & Fedorov, 2017). Analysis of the MioMIP1 models suggests mean tropical SST continues to increase at higher $CO_2$ concentrations (Burls et al., 2021) and potentially the presence of a permanent El Niño in the high $CO_2$ MioMIP1 simulations. Ultimately, shifts in tropical SST patterns could imprint teleconnection precipitation patterns (Fedorov et al., 2006; Goldner et al., 2011; Molnar & Cane, 2007) in our analysis. Lastly, more rigorous regional studies and at higher model resolution (Acosta & Huber, 2017; Kiehl et al., 2021; Shields et al., 2021), for example, the breakdown of multiple and more appropriate climate zones could yield better model-data agreement.

Our analysis found strengths and weaknesses when using a MIP of opportunity approach and highlighted considerable actions for the next iteration of MioMIP. The differences in paleogeography enable the investigation of
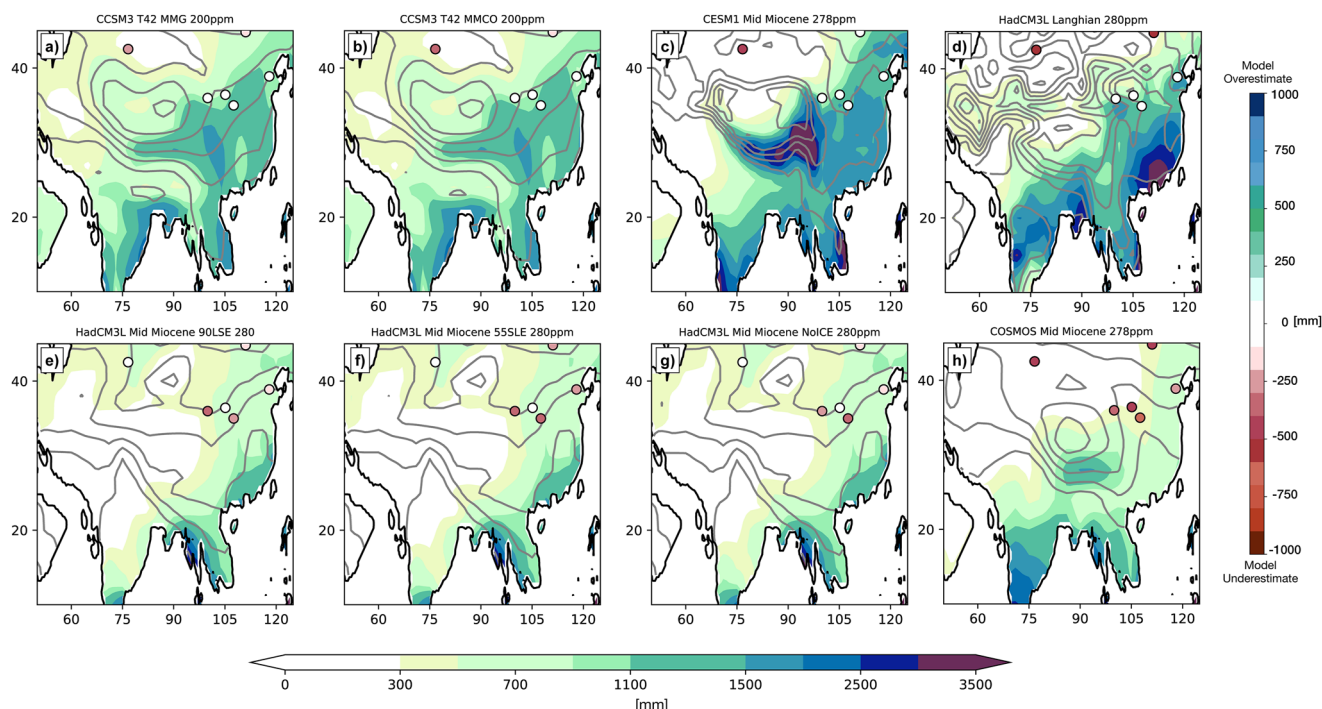
**Figure 18.** Regional terrestrial mean annual precipitation (MAP) (mm/year) over Asia, overlain with contours of surface temperature to illustrate region of high topography and point-wise and model-data comparison showing MAP bias (mm).

non-$CO_2$ parameters on the hydroclimate and highlight robust changes when $CO_2$ concentrations were modified. However, we also found using a MIP of opportunity to be a source of uncertainty in MioMIP1 model-data comparison and presented substantial inter-model differences. For example, changes in the plate tectonics reconstruction (Lunt et al., 2016), such as gateways (Tethys Sea, Central American Seaway, and Greenland-Scotland Ridge) and large continental wetland systems, have an immense impact on local heat and moisture distribution (Bradshaw et al., 2021; Frigola et al., 2018, 2021; Fu et al., 2021; Goldner et al., 2014; Jeffery et al., 2012; Knorr & Lohmann, 2014; Stärz et al., 2017). Model-data discrepancy near regions with variable paleotopography identified key regions that should be focused on for the next MioMIP, which will likely require greater model resolution to fully resolve (Acosta & Huber, 2020; Botsyun et al., 2022; Kiehl et al., 2021; Shields et al., 2021). Changes to the land ice-sheets (Bradshaw et al., 2021; Frigola et al., 2021; Gasson et al., 2016; Goldner et al., 2013; Paxman et al., 2019), the use of newer cloud microphysics schemes (Carmichael et al., 2016; Erfani & Burls, 2019; Heavens et al., 2012; Sagoo & Storelvmo, 2017), implementation of different vegetation and soil properties (Acosta et al., 2022; Bradshaw et al., 2015, 2012; Tabor et al., 2020; Zhou et al., 2018), and accurately capturing ocean circulation (e.g., regional SST distribution) all have the ability to modify the global energy balance, radiative feedbacks, and plays a role in governing the hydrological cycle. Nevertheless, ascertaining accurate MioMIP model boundary conditions (e.g., topography, land-ice, vegetation distribution) is still an active research area, especially since such processes are dynamic, can span over several millions of years, and thus have their own sets of uncertainties.

Terrestrial climate proxies also have their own set of uncertainties associated with them. For example, terrestrial proxies can have poorly constrained dating that can be derived from basin-wide stratigraphic correlation, leading to some locations having less accurate age constraints (Botsyun et al., 2022). In the current dataset, 28 locations have a dating uncertainty of <1 Ma, whereas 48 sites have an age range of >2 Ma (see Burls et al. (2021) and Supplementary dataset). Sub-orbital timescales are a challenge in the terrestrial record, but have been achieved at limited sites (Höfig et al., 2021). Current precipitation reconstructions overwhelmingly rely on the co-existence approach (78 locations), which can only produce a range of equally valid values rather than a mean with uncertainty and has known sources of internal uncertainty (Utescher et al., 2014). However, initial work using probability density function reconstructions shows the coexistence approach provides an optimum range of uncertainty that has been found to be comparable with climate reconstructions (Gibson et al., 2022).

Further, nearest living relative-based approaches, such as the coexistence approach, compare well against zoological reconstructions (Böhme et al., 2011; Eronen et al., 2011), geochemical techniques (Adams et al., 2011; Gibson et al., 2022; Klages et al., 2020; Stein et al., 2021), and physiognomic approaches (Fletcher et al., 2014). Additionally, fossil floras from dry and arid conditions could be underrepresented compared to those found under humid environments (Bruch et al., 2011). While, although limited, the current middle Miocene biome reconstruction presented here does include some arid floras on all continents except Australia (Pound et al., 2012; Steinthorsdottir et al., 2021), it is not currently known if the depicted wetter environment is a feature of a globally humid middle Miocene or a bias in the paleobotanical record. Thus, the incorporation of alternative hydroclimate proxies (including 10 sites already in the dataset that aren't based on the coexistence approach), such as water isotopes (Kukla et al., 2019), soil carbon isotopes (Stein et al., 2021), leaf wax n-alkanes (Feakins et al., 2020), and zoological proxies reconstructions (Böhme et al., 2011; Eronen et al., 2011), and additional water isotope modeling capabilities should lead to more robust model-data comparisons.

When considering the implications of our study and those of other elevated $CO_2$ climates, such as the Pliocene and Eocene, for future hydroclimate projections, one has to be mindful that transient and equilibrium responses to global warming will differ. In particular, oceanic and land-surface adjustment on decadal to centennial timescales for the surface-driven circulation and millennial timescales for the thermohaline circulation will result in the delayed adjustment of large-scale surface temperature gradients with implications for the hydrological cycle (e.g., Lehner & Coats, 2021; Sniderman et al., 2019; Zhu et al., 2023). Nevertheless, our Miocene model-data comparison suggests that future projections near equilibrium may be underestimating the degree of mid- and high-latitude wetting and, more speculatively, overestimating the degree of subtropical drying. The majority of the paleobotanical data presented here are much wetter than the multi-model means, as well as most of the individual models (Table 2 and Figure 14). Rapid hydrological changes (years to decadal time-scales) such as climate tipping points and transient modes of variability were not assessed in our study, but nonetheless most likely lean toward an intensified hydrological cycle as the tropics, mid- and high-latitudes become wetter, and the subtropics become drier in response to warming patterns (Douville et al., 2021).

## 5. Conclusion

This study uses the Miocene MIP of opportunity (Burls et al., 2021) to understand the hydrological cycle and its response across models to a range of Miocene boundary conditions, including $CO_2$ forcings. We also presented a comprehensive MAP model-data comparison of early-to-middle (20.03–11.6 Ma) and middle-to-late (11.5–5.33 Ma) Miocene simulations versus paleobotanical proxies to discern how well the MioMIP1 models capture global and regional precipitation patterns. Lastly, we identified crucial elements that impact the hydroclimate patterns, which should be considered for the next MioMIP iteration.

Although given a wide range of different boundary conditions and model configurations, the MioMIP1 exhibits converging features of the hydrological response to systematic planetary warming. We find that the MioMIP models show intensification of the hydrological cycle as we increase $CO_2$ concentrations with a hydrological sensitivity of ∼2% per degree of warming. Our study finds intensification of tropical MAP, including the Southern Hemisphere branch of the ITCZ and many regions of the global monsoon system, at higher GMST. Additionally, we also find, with high model agreement, mid- and high-latitude MAP increasing at higher GMST. Whereas, drying over the subtropics shows low model agreement and identifies a critical region. Despite the enhancement of MAP under warmer conditions, our model-data comparison suggests that the MioMIP1 models underestimate proxy reconstructed estimates overall. Moving forward, future analysis with coordinated boundary conditions, a more subject-focused analysis, for example, the role of uplift on regional precipitation, higher model resolution, land surface change, cloud-aerosol feedback, and the addition of multiple types of terrestrial proxy samples, should help identify mechanisms that explain our findings and improve model-data comparison.

## Data Availability Statements

Synthesis of terrestrial MAP used for Miocene model-data comparison and climate model output for early-to-middle and middle-to-late MioMIP1 simulations with precipitation, evaporation, and surface temperature are found in the Zenodo repository (Acosta et al., 2023). The code used to make the figures is available at GitHub (https://github.com/rpacosta07/MioMIP1_HydrologicalCycle/tree/v1.0.1) (Acosta, 2023).

# References

Acosta, R. P. (2023). MioMIP1 hydrological cycle master code (v1.0.1). Zenodo. https://doi.org/10.5281/zenodo.10285720

Acosta, R. P., Burls, N. J., Pound, M. J., Bradshaw, C. D., De Boer, A. M., Herold, N., et al. (2023). A model-data comparison of the hydrological response to Miocene warmth: Leveraging the MioMIP1 opportunistic multi-model ensemble [Dataset]. Zenodo. https://doi.org/10.5281/zenodo.8132337

Acosta, R. P., & Huber, M. (2017). The neglected Indo-Gangetic Plains low-level jet and its importance for moisture transport and precipitation during the peak summer monsoon. *Geophysical Research Letters*, *44*(16), 8601–8610. https://doi.org/10.1002/2017GL074440

Acosta, R. P., & Huber, M. (2020). Competing topographic mechanisms for the summer Indo-Asian monsoon. *Geophysical Research Letters*, *47*(3), e2019GL085112. https://doi.org/10.1029/2019GL085112

Acosta, R. P., Ladant, J.-B., Zhu, J., & Poulsen, C. J. (2022). Evolution of the Atlantic Intertropical Convergence Zone, and the South American and African monsoons over the past 95-Myr and their impact on the tropical rainforests. *Paleoceanography and Paleoclimatology*, *37*(7), e2021PA004383. https://doi.org/10.1029/2021PA004383

Adams, J. S., Kraus, M. J., & Wing, S. L. (2011). Evaluating the use of weathering indices for determining mean annual precipitation in the ancient stratigraphic record. *Palaeogeography, Palaeoclimatology, Palaeoecology*, *309*(3–4), 358–366. https://doi.org/10.1016/j.palaeo.2011.07.004

Adler, R. F., Huffman, G. J., Chang, A., Ferraro, R., Xie, P.-P., Janowiak, J., et al. (2003). The Version-2 Global Precipitation Climatology project (GPCP) monthly precipitation analysis (1979–present). *Journal of Hydrometeorology*, *4*(6), 1147–1167. https://doi.org/10.1175/1525-7541(2003)004<1147:tvgpcp>2.0.co;2

Allan, R. P., Barlow, M., Byrne, M. P., Cherchi, A., Douville, H., Fowler, H. J., et al. (2020). Advances in understanding large-scale responses of the water cycle to climate change. *Annals of the New York Academy of Sciences*, *1472*(1), 49–75. https://doi.org/10.1111/nyas.14337

Bhattacharya, T., Feng, R., Tierney, J., Burls, N., Knapp, S., & Fu, M. (2022). Expansion and intensification of the North American Monsoon during the Pliocene. *AGU Advances*, *3*(6), e2022AV000757. https://doi.org/10.1029/2022AV000757

Böhme, M., Winklhofer, M., & Ilg, A. (2011). Miocene precipitation in Europe: Temporal trends and spatial gradients. *Palaeogeography, Palaeoclimatology, Palaeoecology*, *304*(3–4), 212–218. https://doi.org/10.1016/j.palaeo.2010.09.028

Botsyun, S., Ehlers, T. A., Koptev, A., Risi, C., Stepanek, C., Mutz, S. G., et al. (2022). Middle Miocene climate and stable oxygen isotopes in Europe based on numerical modeling. *Paleoceanography and Paleoclimatology*, *37*(10), 1–42. https://doi.org/10.1029/2022PA004442

Bradshaw, C. D., Langebroek, P. M., Lear, C. H., Lunt, D. J., Coxall, H. K., Sosdian, S. M., & de Boer, A. M. (2021). Hydrological impact of Middle Miocene Antarctic ice-free areas coupled to deep ocean temperatures. *Nature Geoscience*, *14*(6), 429–436. https://doi.org/10.1038/s41561-021-00745-w

Bradshaw, C. D., Lunt, D. J., Flecker, R., & Davies-Barnard, T. (2015). Disentangling the roles of late Miocene palaeogeography and vegetation – Implications for climate sensitivity. *Palaeogeography, Palaeoclimatology, Palaeoecology*, *417*, 17–34. https://doi.org/10.1016/j.palaeo.2014.10.003

Bradshaw, C. D., Lunt, D. J., Flecker, R., Salzmann, U., Pound, M. J., Haywood, A. M., & Eronen, J. T. (2012). The relative roles of $CO_2$ and palaeogeography in determining late Miocene climate: Results from a terrestrial model-data comparison. *Climate of the Past*, *8*(4), 1257–1285. https://doi.org/10.5194/cp-8-1257-2012

Brierley, C. M., & Fedorov, A. V. (2016). Comparing the impacts of Miocene–Pliocene changes in inter-ocean gateways on climate: Central American Seaway, Bering Strait, and Indonesia. *Earth and Planetary Science Letters*, *444*, 116–130. https://doi.org/10.1016/j.epsl.2016.03.010

Bruch, A. A., Utescher, T., & Mosbrugger, V. (2011). Precipitation patterns in the Miocene of Central Europe and the development of continentality. *Palaeogeography, Palaeoclimatology, Palaeoecology*, *304*(3–4), 202–211. https://doi.org/10.1016/j.palaeo.2010.10.002

Burls, N. J., Bradshaw, C. D., De Boer, A. M., Herold, N., Huber, M., Pound, M., et al. (2021). Simulating Miocene warmth: Insights from an opportunistic Multi-Model Ensemble (MioMIP1). *Paleoceanography and Paleoclimatology*, *36*(5), e2020PA004054. https://doi.org/10.1029/2020pa004054

Burls, N. J., & Fedorov, A. V. (2017). Wetter subtropics in a warmer world: Contrasting past and future hydrological cycles. *Proceedings of the National Academy of Sciences of the United States of America*, *114*(49), 12888–12893. https://doi.org/10.1073/pnas.1703421114

Byrne, M. P., Pendergrass, A. G., Rapp, A. D., & Wodzicki, K. R. (2018). Response of the Intertropical Convergence Zone to climate change: Location, width, and strength. *Current Climate Change Reports*, *4*(4), 355–370. https://doi.org/10.1007/s40641-018-0110-5

Carmichael, M. J., Lunt, D. J., Huber, M., Heinemann, M., Kiehl, J., LeGrande, A., et al. (2016). A model-model and data-model comparison for the early Eocene hydrological cycle. *Climate of the Past*, *12*(2), 455–481. https://doi.org/10.5194/cp-12-455-2016

Cramwinckel, M. J., Burls, N. J., Fahad, A. A., Knapp, S., West, C. K., Reichgelt, T., et al. (2023). Global and zonal-mean hydrological response to early Eocene warmth. *Paleoceanography and Paleoclimatology*, *38*(6), e2022PA004542. https://doi.org/10.1029/2022PA004542

Dicks, A. J. (2019). *Understanding Miocene climatic warmth (Thesis)*. Purdue University Graduate School. https://doi.org/10.25394/PGS.8956736.v1

Douville, H., Raghavan, K., & Renwick, J. (2021). Water cycle changes. In *Climate change 2021: The physical science basis. Contribution of Working Group I to the Sixth Assessment Report of the IPCC* (pp. 1055–1210). https://doi.org/10.1017/9781009157896.010.1055

Erfani, E., & Burls, N. J. (2019). The strength of low-cloud feedbacks and tropical climate: A CESM sensitivity study. *Journal of Climate*, *32*(9), 2497–2516. https://doi.org/10.1175/JCLI-D-18-0551.1

Eronen, J. T., Micheels, A., & Utescher, T. (2011). A comparison of estimates of mean annual precipitation from different proxies: A pilot study for the European Neogene. *Evolutionary Ecology Research*, *13*(8), 851–867.

Farnsworth, A., Lunt, D. J., O'Brien, C. L., Foster, G. L., Inglis, G. N., Markwick, P., et al. (2019a). Climate sensitivity on geological timescales controlled by nonlinear feedbacks and ocean circulation. *Geophysical Research Letters*, *46*(16), 9880–9889. https://doi.org/10.1029/2019GL083574

Farnsworth, A., Lunt, D., Robinson, S., Valdes, P., Roberts, W., Clift, P., et al. (2019b). Past East Asian monsoon evolution controlled by palaeogeography, not $CO_2$. *Science Advances*, *5*(10), 1–14. https://doi.org/10.1126/sciadv.aax1697

Feakins, S. J., Liddy, H. M., Tauxe, L., Galy, V., Feng, X., Tierney, J. E., et al. (2020). Miocene $C_4$ grassland expansion as recorded by the Indus Fan. *Paleoceanography and Paleoclimatology*, *35*(6), 1–18. https://doi.org/10.1029/2020PA003856

Fedorov, A. V., Burls, N. J., Lawrence, K. T., & Peterson, L. C. (2015). Tightly linked zonal and meridional sea surface temperature gradients over the past five million years. *Nature Geoscience*, *8*(12), 975–980. https://doi.org/10.1038/ngeo2577

Fedorov, A. V., Dekens, P. S., McCarthy, M., Ravelo, A. C., DeMenocal, P. B., Barreiro, M., et al. (2006). The Pliocene paradox (mechanisms for a permanent El Niño). *Science*, *312*(5779), 1485–1489. https://doi.org/10.1126/science.1122666

Fletcher, T. L., Greenwood, D. R., Moss, P. T., & Salisbury, S. W. (2014). Paleoclimate of the late cretaceous (Cenomanian-Turonian) portion of the Winton formation, central-western Queensland, Australia: New observations based on clamp and bioclimatic analysis. *PALAIOS*, *29*(3), 121–128. https://doi.org/10.2110/palo.2013.080

Frieling, J., Gebhardt, H., Huber, M., Adekeye, O. A., Akande, S. O., Reichart, G., et al. (2017). Extreme warmth and heat-stressed plankton in the tropics during the Paleocene-Eocene Thermal Maximum. *Science Advances*, *3*(3). https://doi.org/10.1126/sciadv.160089

Frigola, A., Prange, M., & Schulz, M. (2018). Boundary conditions for the Middle Miocene Climate Transition (MMCT v1.0). *Geoscientific Model Development*, *11*(4), 1607–1626. https://doi.org/10.5194/gmd-11-1607-2018

Frigola, A., Prange, M., & Schulz, M. (2021). A dynamic ocean driven by changes in $CO_2$ and Antarctic ice-sheet in the middle Miocene. *Palaeogeography, Palaeoclimatology, Palaeoecology*, *579*, 110591. https://doi.org/10.1016/j.palaeo.2021.110591

Fu, M., Cane, M. A., Molnar, P., & Tziperman, E. (2021). Wetter subtropics lead to reduced Pliocene coastal upwelling. *Paleoceanography and Paleoclimatology*, *36*(10), 1–22. https://doi.org/10.1029/2021PA004243

Gaskell, D. E., Huber, M., O'Brien, C. L., Inglis, G. N., Acosta, R. P., Poulsen, C. J., & Hull, P. M. (2022). The latitudinal temperature gradient and its climate dependence as inferred from foraminiferal δ18O over the past 95 million years. *Proceedings of the National Academy of Sciences*, *119*(11), 1–8. https://doi.org/10.1073/pnas.2111332119/-/DCSupplemental.Published

Gasson, E., DeConto, R. M., Pollard, D., & Levy, R. H. (2016). Dynamic Antarctic ice sheet during the early to mid-Miocene. *Proceedings of the National Academy of Sciences of the United States of America*, *113*(13), 3459–3464. https://doi.org/10.1073/pnas.1516130113

Geen, R., Bordoni, S., Battisti, D. S., & Hui, K. (2020). Monsoons, ITCZs and the concept of the global monsoon. *Reviews of Geophysics*, *58*(4), 1–45. https://doi.org/10.1029/2020rg000700

Gibson, M. E., McCoy, J., O'Keefe, J. M. K., Otaño, N. B. N., Warny, S., & Pound, M. J. (2022). Reconstructing terrestrial paleoclimates: A comparison of the co-existence approach, Bayesian and probability reconstruction techniques using the UK Neogene. *Paleoceanography and Paleoclimatology*, *37*(2), 1–18. https://doi.org/10.1029/2021PA004358

Goldner, A., Herold, N., & Huber, M. (2014). The challenge of simulating the warmth of the mid-Miocene climatic optimum in CESM1. *Climate of the Past*, *10*(2), 523–536. https://doi.org/10.5194/cp-10-523-2014

Goldner, A., Huber, M., & Caballero, R. (2013). Does Antarctic glaciation cool the world? *Climate of the Past*, *9*(1), 173–189. https://doi.org/10.5194/cp-9-173-2013

Goldner, A., Huber, M., Diffenbaugh, N., & Caballero, R. (2011). Implications of the permanent El Niño teleconnection "blueprint" for past global and North American hydroclimatology. *Climate of the Past*, *7*(3), 723–743. https://doi.org/10.5194/cp-7-723-2011

Han, Z., Zhang, Q., Li, Q., Feng, R., Haywood, A. M., Tindall, J. C., et al. (2021). Evaluating the large-scale hydrological cycle response within the Pliocene Model Intercomparison Project Phase 2 (PlioMIP2) ensemble. *Climate of the Past*, *17*(6), 2537–2558. https://doi.org/10.5194/cp-17-2537-2021

Heavens, N. G., Shields, C. A., & Mahowald, N. M. (2012). A paleogeographic approach to aerosol prescription in simulations of deep time climate. *Journal of Advances in Modeling Earth Systems*, *4*(11), 1–13. https://doi.org/10.1029/2012MS000166

Held, I. M., & Soden, B. J. (2006). Robust responses of the hydrological cycle to global warming. *Journal of Climate*, *19*(21), 5686–5699. https://doi.org/10.1175/jcli3990.1

Herbert, T. D., Dalton, C. A., Liu, Z., Salazar, A., Si, W., & Wilson, D. S. (2022). Tectonic degassing drove global temperature trends since 20 Ma. *Science*, *377*(6601), 116–119. https://doi.org/10.1126/science.abl4353

Herold, N., Huber, M., & Müller, R. D. (2011). Modeling the Miocene climatic optimum. Part I: Land and atmosphere. *Journal of Climate*, *24*(24), 6353–6372. https://doi.org/10.1175/2011jcli4035.1

Herold, N., Müller, R. D., & Seton, M. (2010). Comparing early to middle Miocene terrestrial climate simulations with geological data. *Geosphere*, *6*(6), 952–961. https://doi.org/10.1130/ges00544.1

Höfig, D., Zhang, Y. G., Giosan, L., Leng, Q., Liang, J., Wu, M., et al. (2021). Annually resolved sediments in the classic Clarkia lacustrine deposits (Idaho, USA) during the middle Miocene Climate Optimum. *Geology*, *49*(8), 916–920.

Huber, M., & Caballero, R. (2011). The early Eocene equable climate problem revisited. *Climate of the Past*, *7*(2), 603–633. https://doi.org/10.5194/cp-7-603-2011

Jaramillo, C., Hoorn, C., Silva, S. A. F., Leite, F., Herrera, F., Quiroz, L., et al. (2010). The origin of the modern Amazon rainforest: Implications of the palynological and palaeobotanical record. In *Amazonia, landscape and species evolution: A look into the past* (pp. 317–334). Wiley. https://doi.org/10.1002/9781444306408.ch19

Jeffery, L. M., Poulsen, C. J., & Ehlers, T. A. (2012). Impacts of Cenozoic global cooling, surface uplift, and an inland seaway on South American paleoclimate and precipitation δ18O. *Bulletin of the Geological Society of America*, *124*(3–4), 335–351. https://doi.org/10.1130/B30480.1

Kiehl, J. T., Zarzycki, C. M., Shields, C. A., & Rothstein, M. V. (2021). Simulated changes to tropical cyclones across the Paleocene-Eocene Thermal Maximum (PETM) boundary. *Palaeogeography, Palaeoclimatology, Palaeoecology*, *572*, 110421. https://doi.org/10.1016/j.palaeo.2021.110421

Klages, J. P., Salzmann, U., Bickert, T., Hillenbrand, C. D., Gohl, K., Kuhn, G., et al. (2020). Temperate rainforests near the South Pole during peak Cretaceous warmth. *Nature*, *580*(7801), 81–86. https://doi.org/10.1038/s41586-020-2148-5

Knorr, G., Butzin, M., Micheels, A., & Lohmann, G. (2011). A warm Miocene climate at low atmospheric $CO_2$ levels. *Geophysical Research Letters*, *38*(20), 1–5. https://doi.org/10.1029/2011GL048873

Knorr, G., & Lohmann, G. (2014). Climate warming during Antarctic ice sheet expansion at the middle Miocene transition. *Nature Geoscience*, *7*(5), 376–381. https://doi.org/10.1038/ngeo2119

Kukla, T., Winnick, M. J., Maher, K., Ibarra, D. E., & Chamberlain, C. P. (2019). The sensitivity of terrestrial δ18O gradients to hydroclimate evolution. *Journal of Geophysical Research: Atmospheres*, *124*(2), 563–582. https://doi.org/10.1029/2018JD029571

Ladant, J. B., Donnadieu, Y., Lefebvre, V., & Dumas, C. (2014). The respective role of atmospheric carbon dioxide and orbital parameters on ice sheet evolution at the Eocene-Oligocene transition. *Paleoceanography*, *29*(8), 810–823. https://doi.org/10.1002/2013PA002593

Lehner, F., & Coats, S. (2021). Does regional hydroclimate change scale linearly with global warming? *Geophysical Research Letters*, *48*(23), 1–11. https://doi.org/10.1029/2021GL095127

Lin, J. L. (2007). The double-ITCZ problem in IPCC AR4 coupled GCMs: Ocean-atmosphere feedback analysis. *Journal of Climate*, *20*(18), 4497–4525. https://doi.org/10.1175/jcli4272.1

Liu, X., Huber, M., Foster, G. L., Dessler, A., & Zhang, Y. G. (2022). Persistent high latitude amplification of the Pacific Ocean over the past 10 million years. *Nature Communications*, *13*(1), 1–14. https://doi.org/10.1038/s41467-022-35011-z

Lunt, D. J., Farnsworth, A., Loptson, C., Foster, G. L., Markwick, P., O'Brien, C. L., et al. (2016). Palaeogeographic controls on climate and proxy interpretation. *Climate of the Past*, *12*(5), 1181–1198. https://doi.org/10.5194/cp-12-1181-2016

Lunt, D. J., Jones, T. D., Heinemann, M., Huber, M., LeGrande, A., Winguth, A., et al. (2012). A model-data comparison for a multi-model ensemble of early Eocene atmosphere-ocean simulations: EoMIP. *Climate of the Past*, *8*(5), 1717–1736. https://doi.org/10.5194/cp-8-1717-2012

Mann, M. E. (2021). Beyond the hockey stick: Climate lessons from the Common Era. *Proceedings of the National Academy of Sciences of the United States of America*, *118*(39), e2112797118. https://doi.org/10.1073/pnas.2112797118

Molnar, P., & Cane, M. A. (2007). Early Pliocene (pre-Ice age) El Niño-like global climate: Which El Niño? *Geosphere*, *3*(5), 337–365. https://doi.org/10.1130/GES00103.1

Morley, R. J. (2011). Cretaceous and tertiary climate change and the past distribution of megathermal rainforests. In M. Bush, J. Flenley, & W. Gosling (Eds.), *Tropical rainforest responses to climatic change* (pp. 1–34). Springer. https://doi.org/10.1007/978-3-642-05383-2_1

Oueslati, B., & Bellon, G. (2015). The double ITCZ bias in CMIP5 models: Interaction between SST, large-scale circulation and precipitation. *Climate Dynamics*, *44*, 585–607. https://doi.org/10.1007/s00382-015-2468-6

Pascale, S., Boos, W. R., Bordoni, S., Delworth, T. L., Kapnick, S. B., Murakami, H., et al. (2017). Weakening of the North American monsoon with global warming. *Nature Climate Change*, *7*(11), 806–812. https://doi.org/10.1038/nclimate3412

Paxman, G. J. G., Jamieson, S. S. R., Hochmuth, K., Gohl, K., Bentley, M. J., Leitchenkov, G., & Ferraccioli, F. (2019). Reconstructions of Antarctic topography since the Eocene–Oligocene boundary. *Palaeogeography, Palaeoclimatology, Palaeoecology*, *535*, 109346. https://doi.org/10.1016/j.palaeo.2019.109346

Pendergrass, A. G. (2020). The global-mean precipitation response to $CO_2$-induced warming in CMIP6 models. *Geophysical Research Letters*, *47*(17), 1–10. https://doi.org/10.1029/2020GL089964

Pierrehumbert, R. T. (2002). The hydrologic cycle in deep-time climate problems. *Nature*, *419*(6903), 191–198. https://doi.org/10.1038/nature01088

Pound, M. J., Haywood, A. M., Salzmann, U., & Riding, J. B. (2012). Global vegetation dynamics and latitudinal temperature gradients during the mid to late Miocene (15.97–5.33 Ma). *Earth-Science Reviews*, *112*(1–2), 1–22. https://doi.org/10.1016/j.earscirev.2012.02.005

Pound, M. J., Haywood, A. M., Salzmann, U., Riding, J. B., Lunt, D. J., & Hunter, S. J. (2011). A Tortonian (Late Miocene, 11.61–7.25 Ma) global vegetation reconstruction. *Palaeogeography, Palaeoclimatology, Palaeoecology*, *300*(1–4), 29–45. https://doi.org/10.1016/j.palaeo.2010.11.029

Rae, J. W. B., Zhang, Y. G., Liu, X., Foster, G. L., Stoll, H. M., & Whiteford, R. D. M. (2021). Atmospheric $CO_2$ over the past 66 million years from marine archives. *Annual Review of Earth and Planetary Sciences*, *49*(1), 609–641. https://doi.org/10.1146/annurev-earth-082420-063026

Sagoo, N., & Storelvmo, T. (2017). Testing the sensitivity of past climates to the indirect effects of dust. *Geophysical Research Letters*, *44*(11), 5807–5817. https://doi.org/10.1002/2017GL072584

Sarr, A.-C., Donnadieu, Y., Bolton, C. T., Ladant, J.-B., Licht, A., Fluteau, F., et al. (2022). Neogene South Asian monsoon rainfall and wind histories diverged due to topographic effects. *Nature Geoscience*, *15*, 314–319. https://doi.org/10.1038/s41561-022-00919-0

Sepulchre, P., Caubel, A., Ladant, J. B., Bopp, L., Boucher, O., Braconnot, P., et al. (2020). IPSL-CM5A2 – An Earth system model designed for multi-millennial climate simulations. *Geoscientific Model Development*, *13*(7), 3011–3053. https://doi.org/10.5194/gmd-13-3011-2020

Shields, C. A., Kiehl, J. T., Rush, W., Rothstein, M., & Snyder, M. A. (2021). Atmospheric rivers in high-resolution simulations of the Paleocene Eocene thermal maximum (PETM). *Palaeogeography, Palaeoclimatology, Palaeoecology*, *567*, 110293. https://doi.org/10.1016/j.palaeo.2021.110293

Singh, H. K. A., Bitz, C. M., & Frierson, D. M. W. (2016). The global climate response to lowering surface orography of Antarctica and the importance of atmosphere-ocean coupling. *Journal of Climate*, *29*(11), 4137–4153. https://doi.org/10.1175/JCLI-D-15-0442.1

Sniderman, J. M. K., Brown, J. R., Woodhead, J. D., King, A. D., Gillett, N. P., Tokarska, K. B., et al. (2019). Southern Hemisphere subtropical drying as a transient response to warming. *Nature Climate Change*, *9*(3), 232–236. https://doi.org/10.1038/s41558-019-0397-9

Solomon, S., Plattner, G. K., Knutti, R., & Friedlingstein, P. (2009). Irreversible climate change due to carbon dioxide emissions. *Proceedings of the National Academy of Sciences of the United States of America*, *106*(6), 1704–1709. https://doi.org/10.1073/pnas.0812721106

Spicer, R. A., Yang, J., Spicer, T. E. V., & Farnsworth, A. (2021). Woody dicot leaf traits as a palaeoclimate proxy: 100 years of development and application. *Palaeogeography, Palaeoclimatology, Palaeoecology*, *562*, 110138. https://doi.org/10.1016/j.palaeo.2020.110138

Stärz, M., Jokat, W., Knorr, G., & Lohmann, G. (2017). Threshold in North Atlantic-Arctic ocean circulation controlled by the subsidence of the Greenland-Scotland Ridge. *Nature Communications*, *8*, 1–13. https://doi.org/10.1038/ncomms15681

Stein, R. A., Sheldon, N. D., & Smith, S. Y. (2021). Soil carbon isotope values and paleoprecipitation reconstruction. *Paleoceanography and Paleoclimatology*, *36*(4), 1–18. https://doi.org/10.1029/2020PA004158

Steinthorsdottir, M., Coxall, H. K., de Boer, A. M., Huber, M., Barbolini, N., Bradshaw, C. D., et al. (2021). The Miocene: The future of the past. *Paleoceanography and Paleoclimatology*, *36*(4), e2020PA004037. https://doi.org/10.1029/2020PA004037

Super, J. R., Thomas, E., Pagani, M., Huber, M., O'Brien, C. L., & Hull, P. M. (2020). Miocene evolution of North Atlantic sea surface temperature. *Paleoceanography and Paleoclimatology*, *35*(5), 1–15. https://doi.org/10.1029/2019PA003748

Tabor, C., Otto-Bliesner, B. L., & Liu, Z. (2020). Speleothems of South American and Asian monsoons influenced by a Green Sahara. *Geophysical Research Letters*, *47*(22), 1–11. https://doi.org/10.1029/2020GL089695

Tierney, J. E., Poulsen, C. J., Montañez, I. P., Bhattacharya, T., Feng, R., Ford, H. L., et al. (2020). Past climates inform our future. *Science*, *370*(6517). https://doi.org/10.1126/science.aay3701

Ukkola, A. M., De Kauwe, M. G., Roderick, M. L., Abramowitz, G., & Pitman, A. J. (2020). Robust future changes in meteorological drought in CMIP6 projections despite uncertainty in precipitation. *Geophysical Research Letters*, *47*(11), 1–9. https://doi.org/10.1029/2020GL087820

Utescher, T., Bruch, A. A., Erdei, B., François, L., Ivanov, D., Jacques, F. M. B., et al. (2014). The coexistence approach—Theoretical background and practical considerations of using plant fossils for climate quantification. *Palaeogeography, Palaeoclimatology, Palaeoecology*, *410*, 58–73. https://doi.org/10.1016/j.palaeo.2014.05.031

Wang, B., & Ding, Q. (2006). Changes in global monsoon precipitation over the past 56 years. *Geophysical Research Letters*, *33*(6), L06711. https://doi.org/10.1029/2005GL025347

Westerhold, T., Marwan, N., Drury, A. J., Liebrand, D., Agnini, C., Anagnostou, E., et al. (2020). An astronomically dated record of Earth's climate and its predictability over the last 66 million years. *Science*, *369*(6509), 1383–1388. https://doi.org/10.1126/SCIENCE.ABA6853

Yu, M., Wang, G., Parr, D., & Ahmed, K. F. (2014). Future changes of the terrestrial ecosystem based on a dynamic vegetation model driven with RCP8.5 climate projections from 19 GCMs. *Climatic Change*, *127*(2), 257–271. https://doi.org/10.1007/s10584-014-1249-2

Zhang, Z., Ramstein, G., Schuster, M., Li, C., Contoux, C., & Yan, Q. (2014). Aridification of the Sahara desert caused by Tethys Sea shrinkage during the late Miocene. *Nature*, *513*(7518), 401–404. https://doi.org/10.1038/nature13705

Zhou, H., Helliker, B. R., Huber, M., Dicks, A., & Akçay, E. (2018). C4 photosynthesis and climate through the lens of optimality. *Proceedings of the National Academy of Sciences of the United States of America*, *115*(47), 12057–12062. https://doi.org/10.1073/pnas.1718988115

Zhu, J., Dai, A., Huang, D., Xiao, X., & Liu, Y. (2023). Subtropical drying under greenhouse gas-induced warming. *Climate Dynamics*, *61*, 4219–4242. https://doi.org/10.1007/s00382-023-06797-5

Zhu, J., Otto-Bliesner, B. L., Brady, E. C., Poulsen, C. J., Tierney, J. E., Lofverstrom, M., & DiNezio, P. (2021). Assessment of equilibrium climate sensitivity of the Community Earth System Model version 2 through simulation of the Last Glacial Maximum. *Geophysical Research Letters*, *48*(3), e2020GL091220. https://doi.org/10.1029/2020GL091220

Zhu, J., Poulsen, C. J., Otto-Bliesner, B. L., Liu, Z., Brady, E. C., & Noone, D. (2020). Simulation of early Eocene water isotopes using an Earth system model and its implication for past climate reconstruction. *Earth and Planetary Science Letters*, *537*, 116164. https://doi.org/10.1016/j.epsl.2020.116164